

THE STAR FORMATION RELATION FOR REGIONS IN THE GALACTIC PLANE: THE EFFECT OF SPATIAL RESOLUTION

NALIN VUTISALCHAVAKUL¹, NEAL J. EVANS II¹, CARA BATTERSBY²

Draft version June 20, 2021

ABSTRACT

We examined the relations between molecular gas surface density and star formation rate surface density in a 11 square degree region of the Galactic Plane. Dust continuum at 1.1 mm from the Bolocam Galactic Plane Survey and 22 μm emission from the WISE All-sky survey were used as tracers of molecular gas and star formation rate, respectively, across Galactic longitude of $31.5 \geq l \geq 20.5$ and Galactic latitude of $0.5 \geq b \geq -0.5$. The relation was studied over a range of resolutions from $33''$ to $20'$ by convolving images to larger scales. The pixel-by-pixel correlation between 1.1 mm and 22 μm increases rapidly at small scales and levels off at the scale of $5'-8'$. We studied the star formation relation based on pixel-by-pixel analysis and 1.1 mm and 22 μm peaks analysis. The star formation relation was found to be nearly linear with no significant changes in the form of the relation across all spatial scales and lie above the extragalactic relation from Kennicutt (1998). The average gas depletion time is ≈ 200 Myr and does not change significantly at different scales, but the scatter in the depletion time decreases as the scale increases.

Subject headings: star:formation — ISM: clouds — ISM: dust — infrared: clouds — galaxy: ISM

1. INTRODUCTION

Since star formation is an important process in the formation and evolution of galaxies, understanding what controls the conversion of gas into stars is essential. One of the key parameters in determining the rate of star formation (SFR) in any region should be the amount and nature of the gas available. Our goal is to use surveys of the Galactic Plane to study the relation between gas and star formation on scales ranging from 1 to 200 pc, smaller than the scales accessible in studies of other galaxies.

The study of the relation between gas mass and SFR goes back to the study of Schmidt (1959), who proposed a power law relation between SFR and the gas density. Kennicutt (1998) studied a set of galaxies and found a relation between the disk-averaged SFR surface density (Σ_{SFR}) and gas surface density (Σ_{g}) to be $\Sigma_{\text{SFR}} \propto \Sigma_{\text{g}}^{1.4}$. Since then, there have been many studies on the star formation relation in various types of galaxies, as reviewed by Kennicutt & Evans (2012).

With improvements in instrumental resolution and sensitivity, it became possible to study the relation on smaller scales within individual galaxies (Wong & Blitz 2002). Many studies used high-resolution data to study the relation down to sub-kiloparsec scales (Kennicutt et al. 2007; Bigiel et al. 2008; Blanc et al. 2009; Verley et al. 2010; Liu et al. 2011; Schrubba et al. 2011; Leroy et al. 2013). Star formation has been shown to be associated with molecular gas, rather than total gas (Schruba et al. 2011), and the relations between Σ_{H_2} and Σ_{SFR} tend to be linear ($\Sigma_{\text{SFR}} \propto \Sigma_{\text{H}_2}^{1.0}$) (Bigiel et al. 2008; Leroy et al. 2013). While there is a strong correlation between gas mass and SFR surface density at disk-averaged scales, the relation showed a much larger scatter at smaller

scales, suggesting that the star formation relation breaks down below a certain scale (Onodera et al. 2010; Liu et al. 2011; Schrubba et al. 2010). The large scatter of the star formation relation on small scales implies that the relation does not arise simply from propagating the same relationship up from the scale of individual star forming regions (see Evans et al. 2014). Currently, the extragalactic studies can resolve star forming regions down to sub-kiloparsec scales, with a few reaching scales of about 100 parsec (Schruba et al. 2010; Onodera et al. 2010).

The relations seen in the extragalactic studies are measured on scales that are larger than individual molecular cloud. To understand the physics that underly the relation, one should look at an individual star forming region. To study star formation down to scales of an individual molecular cloud, we need to look at closer regions. Studies of nearby molecular clouds (distance < 1 kpc) have found that star formation was highly concentrated to dense gas (Heiderman et al. 2010; Lada et al. 2010, 2013; Evans et al. 2014). Where star formation happens, the star formation rate lies well above the relation for extragalactic regions, indicating that the extragalactic relation emerges from averaging over both star forming and non-star-forming gas. Regions of high-mass star formation, more representative of what is probed in studies of other galaxies, are generally more distant and require techniques different from those used in the nearby clouds. Studies of massive, dense regions indicated a linear relation between SFR and dense gas (Wu et al. 2005, 2010), similar to those found in other galaxies when tracers of dense gas, like HCN emission were used (Gao & Solomon 2004, a.,). The relation using tracers of dense gas also shows larger Σ_{SFR} at the same Σ_{H_2} than found in extragalactic studies using all the molecular gas.

Extragalactic studies obtain star formation relations by looking at regions covering large areas of the galactic disk while star formation studies in the Milky Way have focused on individual star forming regions that were se-

¹Department of Astronomy, The University of Texas at Austin, 2515 Speedway, Stop C1400, Austin, TX 78712-1205, USA

²Harvard-Smithsonian Center for Astrophysics, 60 Garden St., Cambridge, MA 02138, USA

lected based on certain criteria. The regions studied by Wu et al. (2010) trace small, very dense regions, and they were selected to have signposts of massive star formation and thus may be biased. To bridge the gap between the Galactic and extragalactic scales and to understand some of the differences in the extragalactic results, we need to study Galactic star formation on larger scales and without the biases of previous studies.

There have been many new large scale observations of the Milky Way in various wavelength bands. The Spitzer legacy projects include the MIPS GAL (Carey et al. 2009) and GLIMPSE (Churchwell et al. 2009) surveys, giving a view of the Galactic plane in the infrared from $3.6 \mu\text{m}$ to $70 \mu\text{m}$. All-sky surveys also provide information on star formation rates in the Galactic Plane (e.g., WISE, Wright et al. 2010). The Bolocam Galactic Plane Survey (BGPS) observed the northern part of the Galactic Plane in 1.1 mm dust continuum (Aguirre et al. 2011, Ginsburg et al. 2013 for version 2 of the data). The molecular gas distribution of the Milky Way was studied by Dame et al. (2001) in ^{12}CO and by the Galactic Ring Survey in ^{13}CO (Jackson et al. 2006), with both studies using the $J = 1 \rightarrow 0$ line. With these data available, we can study the relation in a larger area of the Milky Way and perform similar analysis on the Galactic Plane as in the extragalactic data and study how the change in resolution and the change in region selection method affect the result. Understanding the effect of the change in resolution and selection methods will be useful in comparing between Galactic and extragalactic studies.

In this paper, we used the 1.1 mm dust continuum data from the BGPS survey as a molecular gas tracer and $22 \mu\text{m}$ emission from WISE as a tracer of star formation to study the relation between gas mass and star formation for a part of the Galactic Plane. The details of the data used in this study are described in §2, and the data processing is described in §3. We studied the relation between 1.1 mm and $22 \mu\text{m}$ emission by first looking at the pixel-by-pixel relation (§4) and then by identifying separate sources inside the regions (§5). The discussion of the results is in §6, and the results are summarized in §7.

2. DATA

2.1. Emission at 1.1 mm

Dust emission has been used as a total gas tracer in previous studies by assuming that dust and gas are well-mixed (Leroy et al. 2007; Bolatto et al. 2011). The correlation between gas and dust emission has also been studied by the CO survey (Dame et al. 2001) and the recent PLANCK survey (Ade et al. 2011). Ade et al. (2011) argued that dust emission is optically thin up to a column density of $N_H \approx 10^{26} \text{ cm}^{-2}$ at 1 mm. It is also less sensitive to temperature than the FIR emission. Using dust opacities, a dust-to-gas ratio, and a typical dust temperature, we can estimate the gas mass.

We used the 1.1 mm dust continuum from the BGPS version 2 as a molecular gas tracer. The Bolocam Galactic Plane Survey covers about 170 deg^2 in 1.1 mm continuum at an effective resolution of $33''$ (Aguirre et al. 2011). The 1.1 mm data span the range of Galactic longitude of $-10.5^\circ \leq l \leq 90.5^\circ$ and Galactic latitude of $|b| \leq 0.5^\circ$ with additional coverage in some selected re-

gions (Ginsburg et al. 2013). Extended sources were extracted from the 1.1 mm images to a catalog (Bolocat) using a watershed decomposition algorithm (Rosolowsky et al. 2010; Ginsburg et al. 2013). Follow-up molecular line observations of the sources include $\text{HCO}^+ J = 3 - 2$, $\text{N}_2\text{H}^+ J = 3 - 2$ (Schlingman et al. 2011; Shirley et al. 2013), and $\text{NH}_3(1,1)$, $(2,2)$, and $(3,3)$ inversion transitions (Dunham et al. 2011). Distances to a subset of the bolocat sources are also available (Ellsworth-Bowers et al. 2013; Ellsworth-Bowers et al. 2014). Bolocat sources are relatively dense ($\sim 10^{3.5} \text{ cm}^{-3}$) structures in molecular clouds with angular sizes of $\approx 0.5' - 2'$ (Ginsburg et al. 2013).

Surveys by ground-based instruments at $\lambda \sim 1 \text{ mm}$ lose sensitivity to emission beyond some angular scale because it cannot be separated from atmospheric emission variation. The BGPS maps completely recover emission of up to $80''$ and partially recover emission to $\approx 5'$ (Ginsburg et al. 2013). These surveys thus pick out regions of characteristic *volume* densities, which depend on distance. Dunham et al. (2011) calculated sizes and other properties of a subset of sources and characterized the bolocat sources as cores, clumps, and clouds, with size scales of order 0.1 pc, 1 pc, and 10 pc, respectively, depending on sources' distances. As discussed later, the majority of the structures in the regions we study here correspond to relatively dense ($n \approx 10^{3.5} \text{ cm}^{-3}$) clumps within larger molecular clouds. Battisti & Heyer (2014) extracted ^{13}CO clouds associated with selected BGPS sources with dense gas observations and compared the dust mass with the mass of the parent ^{13}CO clouds. Comparing a total mass of BGPS sources inside GMCs with the mass of the GMC gave a median mass ratio of $0.11_{-0.06}^{+0.12}$. If the mass was restricted to regions with mass surface density higher than $200 M_\odot \text{ pc}^{-2}$, the ratio decreased to $0.07_{-0.05}^{+0.13}$ (Battisti & Heyer 2014). The dense gas mass fraction does not appear to depend on cloud mass or cloud mass surface density. This result shows that the 1.1 mm sources occupy a only a small fraction of mass and volume within the clouds. The maps at 1.1 mm also have a smaller chance of source confusion along the line of sight than does CO, which traces more extended emission from the less dense parts of molecular clouds.

2.2. Emission at 22 μm

Mid-infrared continuum emission has been used as a tracer of SFR. The MIPS GAL survey covers our target region in $24 \mu\text{m}$ MIPS band at a resolution of $6''$. However, the saturation level is too low for the purpose of our large scale study. Instead, we used the Wide-field Infrared Survey Explorer (WISE; Wright et al. 2010) all-sky release images at $22 \mu\text{m}$ as a tracer of star formation. WISE observed the entire sky in multiple exposures in four IR bands at 3.4, 4.6, 12, and $22 \mu\text{m}$ with a resolution of $12.0''$ at $22 \mu\text{m}$. SFR($24 \mu\text{m}$) has been calibrated using the Spitzer MIPS $24 \mu\text{m}$ band. The WISE $22 \mu\text{m}$ band overlaps the MIPS $24 \mu\text{m}$ band with a slightly bluer response curve. The comparison between the two bands show that they are comparable (Jarrett et al. 2011; Anderson et al. 2014). We considered the difference between measurements centered at $22 \mu\text{m}$ and those centered at $24 \mu\text{m}$ to be negligible, so use relations derived for $24 \mu\text{m}$

to calculate star formation rates.

The $22\ \mu\text{m}$ emission comes from dust heated by strong stellar radiation or from transiently-heated small dust grains (Draine et al. 2007; Calzetti et al. 2007). The bright emission peaks are expected to indicate dust concentrations that are heated by high mass stars. The $22\ \mu\text{m}$ emission can then be used to trace the presence of high mass stars and so traces the current star formation activities. We used the $22\ \mu\text{m}$ maps to study the relation between star formation activities and the gas distribution.

To convert the $22\ \mu\text{m}$ emission to SFR however, a conversion factor or a calibration is needed. Several studies calibrated a relation between MIR and SFR using extragalactic data (Calzetti et al. 2007, Calzetti et al. 2010 and references therein). These calibrations were done on extragalactic scales assuming a fully-sampled IMF and a long timescale of constant star formation. These assumptions are not always valid when applied to smaller scales or to regions with low mass or low SFR (Vutisalchavakul & Evans 2013; Kennicutt & Evans 2012). The effect of stochastically sampling of the IMF and the star formation history has been studied quantitatively by da Silva et al. (2012) and da Silva et al. (2014). They did not study the SFR measured from $24\ \mu\text{m}$ emission explicitly, but they did study the SFR measured from the bolometric luminosity, which is the closest in sensitivities to the mid-infrared emission. These two tracers correlate closely (Vutisalchavakul & Evans 2013). The SFR determined from the bolometric luminosity, assuming continuous star formation and an IMF, has a scatter of 0.4 to 0.6 dex for $\text{SFR} < 10^{-4}\ \text{M}_{\odot}\ \text{yr}^{-1}$, and begins to systematically underestimate the actual SFR below $10^{-5}\ \text{M}_{\odot}\ \text{yr}^{-1}$ (da Silva et al. 2014). Vutisalchavakul & Evans (2013) found that total infrared luminosity and $24\ \mu\text{m}$ emission can underestimate SFR by more than an order of magnitude for molecular clouds with $\text{SFR} < 10^{-6}\ \text{M}_{\odot}\ \text{yr}^{-1}$. The effects of stochasticity get smaller as the total SFR of the region increases. For this work, $22\ \mu\text{m}$ can underestimate the SFR on small scales and especially at low surface density but should trace SFR better when we look at larger scales, where we average over multiple star forming regions and toward bright regions with high surface density.

2.3. The Regions Studied

The part of the Galactic plane covered in this study includes a Galactic longitude range of $20.5 \leq l \leq 31.5$ and Galactic latitude range of $|b| \leq 0.5$, a total of $11\ \text{deg}^2$, divided into two equal size regions. Both the $1.1\ \text{mm}$ images from BGPS version 2 and WISE $22\ \mu\text{m}$ images were combined into two separate mosaics using Montage (Jacob et al. 2010) for the purpose of data analysis: region 1 at $20.5 \leq l \leq 26.0$ and region 2 at $26.0 \leq l \leq 31.5$. Figure 1 shows $1.1\ \text{mm}$ and $22\ \mu\text{m}$ images for region 1 in the top two panels and region 2 in the third and fourth panels. All the analysis described in the next section was performed similarly on images for the two regions. The results were then combined for further discussion. The two regions show sources with strong emission at $22\ \mu\text{m}$, including well-studied high mass star forming regions W41 and W42 in region 1 and W43 for region 2 (Benjamin et al. 2005). The end of the Galactic bar should be near the end of region 2 at around $l \approx 28 - 31^{\circ}$

(Benjamin et al. 2005).

3. DATA PROCESSING

3.1. Diffuse IR Background Estimation

The $22\ \mu\text{m}$ images show diffuse background emission that is not necessarily associated with recent star formation. The diffuse (cirrus) infrared emission within our Galaxy has long been observed and studied (Low et al. 1984; Miville-Deschênes et al. 2007; Compiègne et al. 2010). We constructed diffuse emission maps to facilitate removal of the diffuse background in the $22\ \mu\text{m}$ images for photometry and for better comparison with the $1.1\ \text{mm}$ images where large scale emission was automatically removed.

The WISE $22\ \mu\text{m}$ images were convolved to a resolution of $33''$ and aligned to the BGPS images, which were then used for estimating the diffuse emission maps. To capture the variations in the background, we adopted the following method. First, source areas were determined by selecting a $22\ \mu\text{m}$ flux contour level that matched bright $22\ \mu\text{m}$ emission areas when inspected by eye. All pixels inside source areas were masked as source pixels. Second, the images were divided into smaller rectangular subgrids at a size of 200 by 200 pixels ($\approx 10.8'$). Iterative applications of Chauvenet's rejection criterion were performed on each subgrid by iteratively applying a 3σ cut until all the remaining pixels are within 3σ of the average pixel value. The average of the remaining pixel values was then taken as the background value for the subgrid. Finally, subgrids with fractions of the source area above a certain clipping threshold were omitted. The rest of the subgrid's background values were interpolated with a thin plate spline interpolation to create a final background image.

This method gave a reasonable representation of the diffuse emission as seen in the original $22\ \mu\text{m}$ images. We chose a source contour level, a grid size, and a clipping threshold that resulted in the closest approximation of the diffuse emission when inspected by eye. Our method gives a diffuse background image that is similar to the method of Battersby et al. (2011). More detailed descriptions on the parameters chosen and the associated uncertainties are provided in Appendix B, while the comparison between two background subtraction methods is provided in Appendix C. The background-subtracted $22\ \mu\text{m}$ images were used for the image convolution.

The result of removing diffuse emission is shown in Figure 2 by comparing the fraction of the estimated diffuse emission to total emission as a function of surface brightness. The diffuse emission dominates the $22\ \mu\text{m}$ flux at low surface brightness and contributes a considerable fraction up to a surface brightness of $\approx 700\ \text{MJy}\ \text{sr}^{-1}$ where the diffuse emission accounts for 50% of the total emission, showing that removing diffuse emission is crucial.

3.2. Image Convolution

The original resolutions of the $1.1\ \text{mm}$ and $22\ \mu\text{m}$ images were $33''$ and $12''$ respectively. Since we intended to study the relations between $1.1\ \text{mm}$ and $22\ \mu\text{m}$ at different scales, we first created a set of images at different spatial resolutions. This was done by convolving the images with a 2D Gaussian profile of varying FWHM.

Both the 22 μm and 1.1 mm images at 33'' resolution were convolved with a 2D Gaussian kernel to resolutions of $\approx 1', 2', 3', 4', 5', 8', 10', 15',$ and 20'. The scale of 20' was the largest scale we could achieve due to the limited coverage of Galactic latitude in the BGPS data. After the convolutions, the convolved images were binned to oversampling rates of ≈ 10 pixels per beam's FWHM. Figure 1 shows the 1.1 mm and 22 μm images at three resolutions: 33'', 10', and 15'. The whole set of the convolved images was then used for further analysis.

3.3. Detection Limit

We identified regions with unreliable detections by estimating the sensitivity levels of both 1.1 mm and 22 μm maps. The sensitivity of the WISE 22 μm images is very low compared to the average flux, and the uncertainty in source emission is dominated by the small scale variations in the diffuse background emission. We estimated the noise in the diffuse emission based on several sky regions in the image at 1' resolution. The average of the standard deviation of all the sky regions was taken as the 1-sigma value of the noise per pixel. The detection limits at other resolutions were estimated by assuming that the noise drops as $1/\sqrt{N_{\text{pixels}}}$, where N_{pixels} is the number of pixels at 1' scale inside a resolution element. Tests on the convolved images supported this assumption.

The RMS noise for the BGPS 1.1 mm maps was estimated in Ginsburg et al. (2013) over the range of the observed Galactic longitude. The average RMS noise in our targeted region ($20.5^\circ < l < 30.5^\circ$) is ≈ 0.0021 Jy per pixel at the original pixel size of 7.2''. Detection limits at other resolutions were estimated under the same assumption as for 22 μm images.

4. RESULTS: PIXEL-BY-PIXEL ANALYSIS

4.1. Correlations between 1.1 mm and 22 μm emission

With the complete set of both 1.1 mm and 22 μm images at various scales, we looked at the correlation between the two. Rank correlation coefficients were calculated between the 1.1 mm and the 22 μm flux per pixel. Rank correlation was used to look at the relation of the data since it is less sensitive to outliers and does not assume a linear relation. The result of the rank correlation coefficients versus resolutions is shown in Figure 3. The blue dots represent data for region 1 while the red dots represent data for region 2. The correlation coefficients for both regions increase rapidly as the scale increases until the scale of $\approx 5'-8'$, above which they appear to be asymptoting to about 0.65 to 0.75, depending on the region. While some differences between the two halves of the data exist, they do not seem large, so we combine the results from both regions in the rest of the paper.

4.2. The Star Formation Relation

With the 1.1 mm and 22 μm flux per pixel, we next converted them to molecular gas surface density (Σ_{H_2}) and SFR surface density (Σ_{SFR}). Since the surface densities are distance independent, we can use the entire regions for sampling data points. The sampling was done by binning the images so that each pixel was approximately equal to a resolution element. Each pixel was then treated as a single data point. This method resulted in non-overlapping regions equal to the resolution

size, covering the entire image, each with a corresponding 1.1 mm and 22 μm flux surface density.

The mass surface density can be calculated from

$$\Sigma_{\text{H}_2} = \left(\frac{S_\nu(1.1)}{\Omega B_\nu(T_{\text{dust}}) \kappa_{\text{dust},1.1}} \right) \left(\frac{\rho_g}{\rho_d} \right), \quad (1)$$

where $S_\nu(1.1 \text{ mm})$ is the 1.1 mm flux density, Ω is the solid angle of a pixel, $\kappa_{\text{dust},1.1} = 1.14 \text{ cm}^2 \text{ g}^{-1}$ is the dust opacity at 1.1 mm per dust mass (Ossenkopf & Henning 1994), and ρ_g/ρ_d is the gas-to-dust mass ratio, taken to be 100 (Hildebrand 1983). Assuming standard values and a dust temperature of 20 K for all sources yields

$$\Sigma_{\text{H}_2} = \frac{37.2 \times S_{1.1\text{mm}}}{\theta_{\text{arcsec}}^2} (\text{g cm}^{-2}), \quad (2)$$

where $S_\nu(1.1\text{mm})$ is the 1.1 mm flux density in Jansky, and θ_{arcsec} is the size of the region in arcsecond (Schlingman et al. 2011).

The SFR surface density was calculated from the extragalactic relation (Calzetti et al. 2007):

$$\Sigma_{\text{SFR}} (M_\odot \text{yr}^{-1} \text{kpc}^{-2}) = 1.56 \times 10^{-35} [S_{24} (\text{ergs s}^{-1} \text{kpc}^{-2})]^{0.8104}. \quad (3)$$

The 24 μm luminosity surface density is described by

$$S_{24} (\text{ergs s}^{-1} \text{kpc}^{-2}) = \frac{\nu (\text{Hz}) L_{24}(\nu) (\text{erg s}^{-1} \text{Hz}^{-1})}{A (\text{kpc}^2)},$$

where $L_{24}(\nu)$ is the 24 μm luminosity per unit frequency, ν is the frequency, and A is the projected physical area of the region. We substituted the 22 μm flux for the 24 μm flux for the calculations.

The resulting Σ_{H_2} and Σ_{SFR} for various spatial scales are shown in Figure 4. The figure shows the star formation relations as contour plots at each resolution. The contours represent number densities of data points of 1, 3, 5, 10, 20, 40, 60, and 80 data points at the binning of 0.2 in $\log(\Sigma_{\text{H}_2})$ and $\log(\Sigma_{\text{SFR}})$. The same color represents the same number density in all the plots. The plot includes all data points with positive fluxes with the vertical and the horizontal dashed red lines representing detection (3-sigma) limits for Σ_{H_2} and Σ_{SFR} respectively. Naturally, the number of data points drops as the scale gets larger, and there are fewer pixels with values < 3-sigma.

The molecular depletion time is defined to be

$$t_{\text{dep}} = \frac{\Sigma_{\text{H}_2}}{\Sigma_{\text{SFR}}}.$$

t_{dep} can be thought of as the timescale for all the molecular gas to be converted into stars at the current rate of star formation. The three dotted lines in Figure 4 show lines of constant depletion time with $t_{\text{dep}} = 10^8, 10^9, 10^{10}$ yr from top to bottom. The distribution of t_{dep} provides a good measure of the scatter in the star formation relations.

Figure 5 shows the distributions of the $\log(t_{\text{dep}})$ at various spatial scales, which include all the data points with positive fluxes. The dashed, blue line in each plot represents a Gaussian fit to the distribution. The result shows that the average $\log(t_{\text{dep}})$ is about 8.3, corresponding to

200 Myr, independent of smoothing length, while the scatter, $\sigma \log(t_{\text{dep}})$, decreases as the smoothing length increases.

The distributions in Figure 5 include many points below the detection limit. To account for the sensitivity issue, we assigned the 3-sigma detection values as upper limits of Σ_{H_2} and Σ_{SFR} for all the data points with values below the detection limits. Data points with upper limits on both Σ_{H_2} and Σ_{SFR} were omitted from further analysis since most of them should be regions not involved in current star formation. Table 1 shows $\langle \log(t_{\text{dep}}) \rangle$ and $\sigma(\log(t_{\text{dep}}))$ estimated by three different methods. The first method (fit) is the Gaussian fit to the distributions of all the data points with positive fluxes before assigning upper limits as shown in Figure 5. The second method (limit) used the data including upper limit values of Σ_{H_2} and Σ_{SFR} to calculate the median and standard deviation of $\log(t_{\text{dep}})$. The third method (EM) used an expectation-maximization algorithm as described in Wolynetz (1979) to estimate the mean and standard deviation of a censored normal distribution. The EM method is based on calculating the maximum likelihood estimates to a distribution assumed to be normally distributed. The data includes left-censored (upper limit in Σ_{H_2}) and right-censored (upper limit in Σ_{SFR}) data points. The uncertainties in the EM method increase for data sets where large fractions of the data points are censored. The three methods give a comparable $\langle \log(t_{\text{dep}}) \rangle$ of about 8.3 regardless of the resolution scale (Table 1). They differ more regarding $\sigma(\log(t_{\text{dep}}))$, but these differences disappear at larger smoothing scales.

5. RESULTS: SOURCE-BASED RELATIONS

The pixel-by-pixel analysis provides a way to study the relation between Σ_{H_2} and Σ_{SFR} for an entire region without a need to extract sources from the images. This method was used in some extragalactic studies (Bigiel et al. 2008; Liu et al. 2011; Leroy et al. 2013). However, the pixel-by-pixel analysis includes regions with low 22 μm and 1.1 mm surface densities that do not necessarily represent star formation. In addition, no information on distance is available.

Another approach to study the relation is to choose regions with strong emission, as was done by some extragalactic studies (e.g., Kennicutt et al. 2007). We started by looking at extracted sources from the BGPS source catalog. These sources also have the advantage of having additional properties determined for a subset of them in previous studies such as distances, sizes, temperature, and densities.

We started with the sources in the BGPS catalog, describing the properties of sources in this sample (§5.1) and study the star formation relation (§5.2). Then we considered what happens when we smoothed the images to larger scales, and extracted data centered on 1.1 mm peaks (§5.3). Finally, we compared these results to those obtained when we extracted data centered on 22 μm peaks (§5.4).

5.1. The BGPS Source Properties

The BGPS source catalog (Bolocat) provides sources extracted from the 1.1 mm images along with integrated source flux and flux inside aperture diameters of 40'', 80'',

and 120''. These sources are possible sites of star formation, and they correspond to cores, clumps, or clouds depending on the distance (Dunham et al. 2011). Since 1.1 mm emission provides an unbiased tracer for dense molecular gas without a pre-selected criteria, Bolocat gives a good set of sources for studying properties of potential star forming regions.

Distances are not available to all the Bolocat sources, but kinematic distances to a subset of sources have been determined by Ellsworth-Bowers et al. (2013); Ellsworth-Bowers et al. (2014) using a Bayesian distance probability distribution function to resolve the kinematic distance ambiguity in the inner Galaxy. The distance catalog provides distances along with the uncertainties. In our targeted regions, 33% of the sources have distances. Figure 6 shows the distance distribution for sources inside our targeted region, where the distances plotted are the maximum likelihood distances from Ellsworth-Bowers et al. (2014). The shaded grey area represents a distance range inside which 90% of the total number of sources reside (see §6.1). The subset of the sources with distances (referred to hereafter as the distance catalog) are generally representative of the entire Bolocat source catalog. Their distribution in Galactic latitude is comparable to that of sources in the full catalog. However, the distance catalog is slightly biased toward sources with larger surface brightness with a median of 6.8 and 8.0 MJy sr⁻¹ for full catalog and distance catalog respectively (see the full discussion in Ellsworth-Bowers et al. 2014).

A fraction of 0.73 of the sources with distances are located in the 5 kpc peak (between 0-7.5 kpc), and a fraction of 0.25 reside near the 10 kpc peaks (between 8-14 kpc) while a very small fraction of sources are at distances around 16 kpc. The mean of the distance is 5.9 kpc, the median is 5.1 kpc, and the standard deviation is 2.8 kpc. We will use the median value to calculate characteristic properties. At 5 kpc, 1 arcminute corresponds to 1.45 pc, and BGPS sources correspond to clumps with typical densities of 10^{3.5} cm⁻³ (Dunham et al. 2010, 2011). The sources at 10-12 kpc are better characterized as clouds, with mean densities below 10³ cm⁻³.

5.2. Analysis Based on Bolocat Sources

We started the investigation at the scale of individual Bolocat sources by looking at the 22 μm emission from these sources. We performed aperture photometry on the 22 μm images of 33'' resolution at each of the Bolocat source positions with an aperture radius of 40'' to compare to the 1.1 mm Bolocat flux of the same aperture size.

The photometry resulted in a total of 1981 Bolocat sources in the whole 11 deg² region; 738 of them have a 22 μm background-subtracted flux below the detection limit, a fraction of 0.37. The photometric uncertainties were determined by combining the observational and Poisson error from the WISE uncertainty maps with the estimated random uncertainties in our method of background subtraction, the details of which can be found in Appendix B.

We next calculated the SFR surface density from the 22 μm flux (Equation 3) and molecular gas surface density from the 1.1 mm flux (Equation 2) within an 80'' aperture. The typical uncertainties are $\approx 28\%$ and 7% for

Σ_{H_2} and Σ_{SFR} respectively. The uncertainties for Σ_{H_2} were determined from the calibration and photometric uncertainties (Ginsburg et al. 2013).

The result is shown in Figure 7. The contours show the source number density, as in Figure 4. The data have a large scatter, with a rank correlation coefficient between $\log(\Sigma_{\text{H}_2})$ and $\log(\Sigma_{\text{SFR}})$ of 0.40. We assumed a power law relation of the form

$$\Sigma_{\text{SFR}} \propto \Sigma_{\text{H}_2}^n, \quad (4)$$

or equivalently

$$\log(\Sigma_{\text{SFR}}) = n \log(\Sigma_{\text{H}_2}) + a. \quad (5)$$

A linear curve fit to the log data including the uncertainties in both axes using MPFITEXY (Markwardt 2009) gave fitting parameters of $n = 0.84 \pm 0.03$ and $a = -2.68 \pm 0.06$, as shown by the solid black line. The dashed red line represents the extragalactic star formation relation from Kennicutt (1998) of

$$\Sigma_{\text{SFR}} = (2.5 \pm 0.7) \times 10^{-4} \Sigma_{\text{H}_2}^{1.4 \pm 0.15}. \quad (6)$$

The vertical and the horizontal dashed lines represent the 3-sigma detection limit, and the dot-dashed blue line represents the relation observed for dense gas as traced by HCN from Wu et al. (2005):

$$(SFR)(M_\odot \text{ yr}^{-1}) \approx 1.2 \times 10^{-8} M_{\text{dense}}(M_\odot). \quad (7)$$

A gaussian fit to the distribution of $\log(t_{\text{dep}})$ gives $\log(t_{\text{dep}}) = 9.0 \pm 0.48$ (≈ 1 Gyr). Including upper limits to Σ_{SFR} , the median $\log(t_{\text{dep}}) = 9.23 \pm 0.69$. The EM method gives the mean of $\log(t_{\text{dep}}) = 9.45 \pm 0.90$.

5.3. Analysis based on 1.1 mm Peaks

On the scale of BGPS sources, the 22 μm emission shows a weak correlation with the 1.1 mm flux with a large scatter. From visual inspections, the 22 μm emission in the whole region is more diffuse than the 1.1 mm emission. A lot of the 22 μm extended emission also does not coincide with the Bolocat source contours. In this section, we studied how the correlation between SFR tracers and gas tracers changes when we look at the regions on larger scales.

Using the images convolved to larger angular scales (§3.2), we identified the local peaks of the 1.1 mm emission. The local peaks were identified by locating pixels whose values are larger than all the adjacent pixels. Overlapping regions were eliminated by dropping peaks with distances to the nearest peak less than the radius of the aperture. We then performed aperture photometry on 22 μm and 1.1 mm images with an aperture centered at the local 1.1 mm peaks and radius equal to the beam's FWHM of the convolved images (aperture radius = 10' for the images convolved to FWHM of 10' and similarly for others). The aperture size was chosen to contain most of the source emission without applying aperture corrections. The same procedures were performed on the images convolved to resolutions of 10', 15', and 20'. Once we go to higher FWHM, the angular source sizes increase, which corresponds to looking at larger physical areas. At a distance of 5 kpc, 20' corresponds to a physical size of about 29 pc in the plane of the sky.

Once we obtained the 1.1 mm and 22 μm fluxes from the photometry, Σ_{H_2} and Σ_{SFR} were calculated using

Equation 2 and 3 respectively. All the data points for the 10', 15', and 20' resolution are above the detection limit in both Σ_{H_2} and Σ_{SFR} . The correlation between $\log(\Sigma_{\text{H}_2})$ and $\log(\Sigma_{\text{SFR}})$ increases from a linear correlation coefficient of 0.66 at 10' scale to 0.76 at 20' scale (Table 2). Two methods of linear curve fit were performed on the data: an unweighted least-squares fit using MPCURVEFIT (Markwardt 2009) and a robust bisector linear fit (IDL Robust_Linefit). The relations for the convolved scales of 10', 15', and 20' can be seen in Figure 8(a). Each data point corresponds to a region inside an aperture centered on a peak of emission in the 1.1 mm image. The solid black line represents the robust fit to the data, the dotted grey line represents the least-square fit to the data, the dashed red line represents the extragalactic star formation relation (Equation 6), and the dot-dashed blue line represents the dense gas relation from Wu et al. (2005). The coefficients of the curve fits are shown in Table 2.

The star formation relations are slightly sub-linear at all scales, more so for the least-squares fit. Both methods show increases in the intercept a (the effective star formation rate) as the scale gets larger.

5.4. Analysis based on 22 μm Peaks

What changes if regions are identified using 22 μm peaks instead of 1.1 mm peaks? To answer that question, we used procedures similar to those used in the 1.1 mm peaks analysis, but we started by identifying local emission peaks in 22 μm images at the resolution of 10', 15', and 20' and performed photometry on both 1.1 mm and 22 μm images at locations of the 22 μm peaks. Figure 8(b) shows the plot of the star formation relation at the three resolution scales. The fit parameters are included in Table 2. The fit parameters are comparable to the parameters for the 1.1 mm peaks.

Initial analysis did not show a significant difference when choosing 22 μm peaks versus choosing 1.1 mm peaks as can be seen from the values of t_{dep} in Table 2. When thresholds were applied to the data however, the result was different. Instead of choosing all the identified local peaks, we chose only bright local peaks by dropping all the regions with fluxes less than 100 signal-to-noise ratio. The approximate values corresponding to these thresholds are $\Sigma_{\text{H}_2} \approx 15 M_\odot \text{ pc}^{-2}$ and $\Sigma_{\text{SFR}} \approx 0.1 M_\odot \text{ yr}^{-1} \text{ kpc}^{-2}$. After the cut, the number of sources are 24, 11, and 6 for the 1.1 mm peaks and 14, 9, and 3 for the 22 μm peaks for the scales of 10', 15', and 20' respectively. Regions with 1.1 mm peaks and 22 μm peaks with fluxes above the threshold were then compared. The result in Figure 9 shows a larger t_{dep} for 1.1 mm peaks than for 22 μm peaks. The difference in t_{dep} decreases as the scale increases. The difference in $\log(t_{\text{dep}})$ is about 0.37 at 5' scale and goes down to about 0.05 at 20' scale. Note, however, that the scatter $\sigma(\log(t_{\text{dep}}))$ is about 0.4 at 5' scale and about 0.2 at 20' scale.

6. DISCUSSION

6.1. Relating to Physical Scales

We have been looking at the relations between gas and star formation at various angular scales. Converting the angular scales to physical scales for our Galactic plane data is different than for resolved extragalactic data since

we are looking edge-on through the disk instead of face-on or nearly face-on. However, the available distances to a subset of the sources can be used to obtain some rough estimations of the physical size that corresponds to each angular resolution. About 33% of the Bolocat sources in our targeted regions have distances measured with a distribution shown in Figure 6 (Ellsworth-Bowers et al. 2014). In estimating the physical scales, we assumed that the distance distribution of these sources is representative of the whole sample (see §5.1).

The first estimation of the physical scale used the median distance to the sources to calculate the size in the plane of the sky. With a median distance of 5.1 kpc, physical sizes in the plane of the sky at different resolutions are shown as the red, dashed line in Figure 10(a). These sizes range from those of clumps to those of clouds. For angular scales small enough to be comparable to an individual source size, the estimated physical scales should represent the physical sizes of the sources.

For comparison to extragalactic measurements, we also computed the typical averaging scale for each resolution, using the distance distribution. The idea behind the method is to use source locations in Galactic latitude and longitude to estimate the solid angle the sources subtend and use the distance distribution to estimate the range of distances for the sources. The result gives the volume subtended by the sources, which can be converted to a length scale. This would represent an upper limit to the relevant scale. To do this, first we binned the distance distribution with a binning size of 0.5 kpc as shown in Figure 6. Three values were chosen as source number density thresholds (per bin) so that the total number of sources above the thresholds account for about 80%, 90%, and 99% of the total sources. This is analogous to drawing number density contours on an image; however, instead of an image, we are drawing one-dimensional contours on a distribution. The shaded-grey area in Figure 6 is an example of the area inside the contour of 90% of the total sources. The resulting distance ranges (δd) are 4.5, 7, and 14 kpc for 80%, 90%, and 99% of the total sources respectively. We calculated an averaging volume (V) for the very long, skinny rectangular prism from

$$\frac{V}{\text{kpc}^3} = \left(\frac{\theta_r}{\text{rad}} \frac{d}{\text{kpc}} \right)^2 \times \frac{\delta d}{\text{kpc}}, \quad (8)$$

where θ_r is the angular size of a resolution element. Reduced to a sphere, the effective radius R is

$$\frac{R}{\text{kpc}} = \left(\frac{3}{4\pi} \frac{V}{\text{kpc}^3} \right)^{1/3}. \quad (9)$$

The effective averaging scale, the diameter ($2R$), at different resolutions is shown in Figure 10(a). Using this estimation at the median distance d of 5.1 kpc, the angular resolution of 20' corresponds to an averaging scale of ≈ 225 pc.

A similar method was used to estimate the number of Bolocat sources each resolution element contains. Bolocat sources were mapped in the Galactic coordinates, and a source number density map was created by counting number of sources inside bin sizes of 0.2° in both axes. Then 2D contours of source number density were drawn on the source number density map to contain ap-

proximately 80%, 90%, and 99% of the total number of sources. The total solid angle inside each contour gave a total area for each completeness value. The average number of sources per resolution element is the solid angle of the resolution element (θ_r^2) divided by the total area for the completeness value times the total number of sources. The average number of sources per resolution element is shown in Figure 10(b). For the larger smoothing lengths, we are typically averaging over 20 to 40 sources.

6.2. The Scatter in the Star Formation Relation

The results on the star formation relations show that the relations at small scales have large scatter as seen in the Bolocat source case or at the small scales in the pixel-by-pixel analysis. The rank correlation coefficients between $\log(\Sigma_{\text{H}_2})$ and $\log(\Sigma_{\text{SFR}})$ increase from 0.40 at the Bolocat source scale to 0.79 at 20' scale for sources based on 1.1 mm peaks. This result is clearly seen in the pixel-by-pixel star formation relation and the distribution of the t_{dep} . The scatter of the t_{dep} in the pixel-by-pixel analysis was estimated by three methods (Table 1), and the results show decreases of $\sigma(\log t_{\text{dep}})$ as the scale gets larger. Figure 11(a) shows the scatter $\sigma(\log t_{\text{dep}})$ over resolution scale for the three methods. At small scales (1' -3'), the EM method gives much larger values of the scatter than the other two methods. At these scales, over 50% of the data are below detection limits, making the estimates of $\sigma(\log t_{\text{dep}})$ uncertain. The three methods give comparable values for scales over 8'.

Figure 11(b) shows a comparison of our results with some resolved extragalactic star formation relations. We used the averaging scale with the 90% distance contour as the maximum relevant scale. We caution that we are comparing across different data sets, and the differences in observations, methodologies, and other factors could contribute in the differences in the scatter of t_{dep} . Our result for the Galactic Plane covers small scales where only few comparable extragalactic data exists to a scale of about 200 pc. The trend from our data suggests a smaller scatter in the depletion time for the Galactic Plane than the extragalactic data.

One important difference in our study is the choice of molecular gas tracers. The BGPS 1.1 mm in general traces denser and smaller parts of molecular clouds than CO or ^{13}CO (Battisti & Heyer 2014). A single GMC can contain multiple 1.1 mm sources. The smaller scatter in our result is consistent with the fact that star formation is more closely associated with denser regions than with the general molecular cloud.

To examine possible causes of the change in the scatter, we looked at contributions to the scatter in $\log t_{\text{dep}}$ ($\sigma(\log t_{\text{dep}})$). Several possible sources of uncertainties in $\log t_{\text{dep}}$ include observational and photometric uncertainties, uncertainties in the parameters assumed in calculating Σ_{SFR} and Σ_{H_2} , uncertainties in the 22 μm flux due to spatial offsets between 1.1mm and 22 μm emission, and a scatter due to variations in intrinsic properties of the sources.

The uncertainties from the observations and the photometry were estimated as the errors associated with the data. The other sources of uncertainties will be discussed below.

6.2.1. Parameter Uncertainties

In the calculation of Σ_{H_2} , we assumed a dust temperature of 20 K, a gas to dust mass ratio of 100, and a dust opacity of $1.14 \text{ cm}^2 \text{ g}^{-1}$ for all the sources following the study of Schlingman et al. (2011). The variations in the real values would contribute to the scatter in Σ_{H_2} . Spectroscopic observations of several molecular lines for Bolocat sources show a median temperature of $\approx 18 \text{ K}$ with a temperature range from 10-30K (Shirley et al. 2013).

In calculating Σ_{SFR} , we used the SFR - $24 \mu\text{m}$ relation (Equation 3) from Calzetti et al. (2007). The calibration was derived assuming a constant SFR on a timescale of 100 Myr and a Kroupa IMF. When applied to an individual molecular cloud or a star forming region, the assumptions cannot always be valid. The timescale assumed for constant star formation is much longer than the average lifetime of molecular clouds (Murray 2011). Several studies show that infrared tracers underestimate SFR with large uncertainties in clouds with low mass or low SFR (Vutisalchavakul & Evans 2013; da Silva et al. 2012; da Silva et al. 2014). The combined effects of stochastically sampling the IMF and the star formation history causes SFR indicators such as $\text{H}\alpha$, FUV, and bolometric luminosity to under-estimate the SFR (da Silva et al. 2014), and the size of the underestimate gets larger as the SFR gets smaller. da Silva et al. (2014) also showed that when stochasticity is taken into account, SFR indicators do not provide a unique value of the SFR.

The variations in the properties of each source contribute to the uncertainties in how well the calculated SFR agrees with the true SFR. This is especially important for the sources with low Σ_{SFR} in our data. As discussed earlier in §2.2, infrared luminosity starts to underestimate SFR below $10^{-5} \text{ M}_{\odot} \text{ yr}^{-1}$ (da Silva et al. 2014). Using the averaging scales with a distance contour of 90%, we estimated the corresponding Σ_{SFR} by assuming a projected area of πR^2 . The value of SFR translates to $\Sigma_{\text{SFR}} \approx 1.4 \times 10^{-2} \text{ M}_{\odot} \text{ yr}^{-1}$ at $1'$ scale, $3.1 \times 10^{-3} \text{ M}_{\odot} \text{ yr}^{-1}$ at $3'$ scale, and $1.6 \times 10^{-3} \text{ M}_{\odot} \text{ yr}^{-1}$ at $5'$ scale. Comparing these values to our results from the pixel-by-pixel analysis (Figure 4) shows that some fractions of the data points at $1'$ - $3'$ scales are below the values, so they are affected by the bias in Σ_{SFR} . Above $5'$ scale, all the data points are above the bias values for both pixel-by-pixel and source based results.

The method of choosing regions also affects the uncertainty introduced by IR as a SFR tracer. Pixel-by-pixel analysis is affected the most since the data contain regions with low Σ_{H_2} and low Σ_{SFR} . Regions chosen by identifying bright emission peaks will show less variations since these regions were chosen based on assumption of strong emission. Therefore, SFR measurements from infrared tracers are more reliable when applied to regions with strong IR emission peaks as in Figure 9. For extragalactic studies, this effect will be more important in line-of-sight (pixel-by-pixel) studies than in studies with CO, $\text{H}\alpha$, or IR peaks.

6.2.2. Spatial offsets between IR and 1.1 mm

The 1.1 mm emission comes from cold dust from dense molecular gas regions in GMCs while the $22 \mu\text{m}$ emission should be dominated by warmer dust heated by stellar

radiation. The two emitting regions might not perfectly coincide spatially with each other. The sizes of the emitting regions could also be different for 1.1 mm and $22 \mu\text{m}$. These two factors will result in spatial offsets, contributing to the scatter in the star formation relation if the scale size is smaller than a typical offset.

If there is a general offset between the $22 \mu\text{m}$ and 1.1 mm sources, the pixel-by-pixel correlation between the two images should get better once the spatial resolution becomes larger than the offset. From Figure 3, the correlation increases rapidly at small scales until they level off at around $5\text{-}8'$ scale. This result suggests that there is an offset of small scale variations between $22 \mu\text{m}$ and 1.1 mm emission of about $5\text{-}8'$, corresponding to 7 to 12 pc at the median distance of 5.1 kpc. This offset is typical of cloud sizes, consistent with the idea that the 1.1 mm source may be a remnant clump, while the infrared emission traces star formation in a now-destroyed clump in the same cloud.

For the case of the Bolocat sources, t_{dep} from the data is greater than the average t_{dep} at larger scales. The t_{dep} of $\approx 1 \text{ Gyr}$ is close to the average values found in extragalactic studies (Wong & Blitz 2002; Leroy et al. 2013). The $22 \mu\text{m}$ flux for each 1.1 mm source was calculated by centering the photometry aperture on the center of the 1.1 mm source. If the infrared emission associated with the 1.1 mm sources does not coincide with the 1.1 mm peak then the estimated $22 \mu\text{m}$ flux would not be representative of the total emission. The infrared emission could also be more extended than the size of the aperture used in the photometry, in which case we would be underestimating the SFR.

To investigate this issue, we looked at the $22 \mu\text{m}$ emission for several sources from the images. One of the sources we tested was G23.95+0.16, which is a massive dense clump with an observed water maser. This source had previously been studied by Wu et al. (2010); Vutisalchavakul & Evans (2013). The source size obtained by fitting a 1D Gaussian is about $3.9'$, much larger than our aperture size of $80''$. A large fraction of the IR emission lies outside the aperture resulting in an underestimated SFR. However this particular source has high Σ_{H_2} and Σ_{SFR} compared to the whole sample. We looked at several other 1.1 mm sources for which there are associated $22 \mu\text{m}$ emission and found that most of the $22 \mu\text{m}$ emission is more extended than the aperture size. To see how much this issue affected the star formation relation result, we performed the photometry again with a larger aperture size of $160''$. The result shows a higher average Σ_{SFR} , and the relation now lies above the Kennicutt (1998) relation.

6.2.3. Intrinsic Source Properties

Aside from the uncertainties already discussed, the scatter in the star formation relation can also be contributed by intrinsic variations in the relation itself. If the SFR for each source is not determined only by the amount of gas available, then we would not expect to see a tight correlation between the two. Our results show a much larger scatter at small scales than do the relations found in disk-average studies. What causes the difference? These 1.1 mm sources are expected to be star forming regions. Then these star forming regions should have variations in their properties. The sources that are

in earlier stages of star formation would contain a large amount of gas and little infrared emission from star formation (large t_{dep}), while the sources that are in later stages of star formation would contain less gas due to gas depletions and emit more strongly in the IR due to stars and current star formation (small t_{dep}). Battersby et al. (2010) found some of the 1.1 mm sources to be infrared dark clouds (IRDC). They are in an early stage of star formation, which would show little or no SFR. If the 1.1 mm sources are in different evolutionary stages, then they will show a large scatter in the star formation relation at the scale of individual sources. Sampling a larger number of individual regions at different stages averages out the scatter in t_{dep} , resulting in a decrease in the scatter in the relation.

The effect of sampling different stages of star formation on the star formation relation has been a topic of several recent studies (Onodera et al. 2010; Schrubba et al. 2010; Leroy et al. 2013; Kruijssen & Longmore 2014). Schrubba et al. (2010) showed, in a study of star formation in M33 at the scale of 75 to 1200 pc, that the choice of CO or H α peaks as centers gave different values of t_{dep} . The difference between the t_{dep} from CO and H α peaks decreases as the aperture size increases. They argued that the dependence of t_{dep} on scale was mainly due to the effect of sampling different evolutionary stages. Kruijssen & Longmore (2014) constructed a model to describe the dependence of t_{dep} and the scatter in t_{dep} on spatial scales and how the differences between t_{dep} when choosing regions on either gas or star formation tracer peaks can be used to estimate the timescales involved in star formation processes.

We found similar results when comparing regions centered on 1.1 mm peaks with regions centered on 22 μm peaks. Regions with strong 1.1 mm emission are more likely to be at an earlier stage of star formation where there is still a large amount of gas while regions with strong 22 μm have already formed stars. The differences in the average t_{dep} between choosing different peaks shown in Figure 9 support the hypothesis that the differences in the stage of star formation contribute to the large scatter in the star formation relation at small scales.

All the mentioned sources of scatter can affect the relations between Σ_{SFR} and Σ_{H_2} . To quantitatively explain the observed data with these uncertainties requires a careful modeling of how each source of scatter depends on scale, which is beyond the scope of this paper. Future studies of properties of individual star forming regions, especially their evolutionary stages, will provide more insights into the problem.

6.3. The Star Formation Relation and Depletion Times

Aside from looking at the scatter in the relation, we can also look for changes in the form of the star formation relation as the resolution is changed. While the correlation improves with averaging scale, the changes to the fitted values for the slope and intercept are not very significant. The star formation relations at all scales are slightly sub-linear and lie between the extragalactic relation from Kennicutt (1998) and the dense gas relation of Wu et al. (2005).

The typical depletion time, both from the pixel-by-pixel analysis and from the source-based analysis with large averaging scales is 200 Myr. The Bolocat source-based analysis shows a larger t_{dep} of about 1 Gyr, closer to the typical extragalactic value. However, this value is very likely an overestimation. As discussed in §6.2.2, the Σ_{SFR} for the Bolocat sources are underestimated due to both the fact that not all the infrared emission was inside the aperture and the bias from using 22 μm to trace SFR for low mass sources. For this analysis we also centered the apertures on Bolocat source, which are bright 1.1 mm regions, so the analysis biases toward larger t_{dep} .

The pixel-by-pixel analysis does not show variations in the average t_{dep} over resolution scales. When all the regions are sampled, t_{dep} can be described reasonably well with log-normal distributions centered at $\approx 10^{8.3}$ yr. Choosing bright 22 μm regions is equivalent to sampling the lower tail of the distribution of t_{dep} , while choosing bright 1.1 mm regions is equivalent to sampling the higher tail of the distribution, resulting in the differences in t_{dep} as seen in Figure 9. Evidently, the method of choosing regions affects the result of t_{dep} , as does the method of identifying local emission peaks. Before making the cut in the 22 μm and 1.1 mm flux, the data did not show a clear trend in t_{dep} over spatial scale. This is likely due to the fact that without the cut, all the identified regions were included. The lower brightness regions tend to sample near the center of the t_{dep} distribution, therefore lowering the distinction between IR or mm peaks. Data for other galaxies could be affected as well since the sensitivity limit varies between data sets.

The constant timescale of 200 Myr seen throughout our data set is similar to the mean value found in the nearby clouds, but about 5 times greater than that found for the dense gas ($A_V > 8$ mag) in the nearby clouds (Evans et al. 2014). Since the 1.1 mm emission is mostly tracing clumps with $\langle n \rangle \approx 10^{3.5} \text{ cm}^{-3}$, similar to the mean density within the $A_V > 8$ mag contours (Evans et al. 2014), this difference may indicate a systematic underestimate of the star formation rate from the 22 μm emission. Individual YSOs could be counted in the nearby clouds, rather than relying on the 22 μm emission. Vutisalchavakul & Evans (2013) showed that the mid-infrared emission does underestimate star formation rate in the nearby clouds where high-mass stars are rare. For this reason we believe that the actual value of t_{dep} is likely overestimated.

On the other hand, the likely overestimated value we get for t_{dep} is already 5 times *smaller* than that found in other galaxies. The BGPS 1.1 mm emission we used in this study traces denser gas than the common tracers used for other galaxies. The 1.1 mm emission only traces about 11% of the gas traced by ^{13}CO , a more typical gas tracer in extragalactic studies (Battisti & Heyer 2014). Therefore, we would expect the average t_{dep} to be smaller than extragalactic values. As a result of these systematic issues, these data tend to lie between the Kennicutt relations for total gas and the Wu relation for even denser ($\langle n \rangle = 10^{4.5} \text{ cm}^{-3}$) gas (Wu et al. 2005).

7. SUMMARY

We studied the relationship between molecular gas and SFR surface density for 11 deg 2 of the Galactic Plane.

The 1.1 mm data from the Bolocam Galactic Plane Survey, which traces dense gas inside molecular clouds, was used as a tracer of molecular gas while 22 μm data from the WISE All-Sky survey was used to trace SFR. We studied the relation from the scale of 33'' to the largest scale of 20' by convolving images with Gaussian beams. We started by looking at the correlations between 22 μm and 1.1 mm images pixel-by-pixel and found that the rank correlation coefficient increases rapidly as scale size increases, leveling off at the scale of about 5'-8'. The 22 μm and 1.1 mm emission are already well correlated at the scale of 5' and the correlations do not change much at larger scales, suggesting a spatial offset or small scale variations around this scale, which corresponds to estimated physical scales of 7-12 pc.

We studied the star formation relations both by analyzing pixel-by-pixel values and by identifying 1.1 mm and 22 μm peaks. The star formation relations from the pixel-by-pixel analysis show close to linear relations. The distribution of t_{dep} can be closely represented as a log-normal with the average of about 200 Myr regardless of the resolution. The relation on small scales shows large scatter, and the scatter decreases as the scale gets larger. The scatter of the $\log(t_{\text{dep}})$ decreases from above 0.6 at 1' scale to about 0.28 at 20' scale. The typical depletion times lie between those for dense clumps and those for total gas or for molecular gas in other galaxies.

For sources centered at 1.1 mm peaks, we found a weak correlation between Σ_{SFR} and Σ_{H_2} at 1.1 mm source scale (aperture diameter of 80''). The correlation gets better at larger scales similarly for 1.1 mm peaks and 22 μm peaks. There are no significant differences in the form of the relation at different scales or when comparing 1.1 mm to 22 μm peaks. The star formation relations at all

scales are slightly sublinear and lie above the extragalactic relation from Kennicutt (1998). When selecting only bright peaks however, the average t_{dep} from centering at 1.1 mm peaks is larger than the average t_{dep} from centering at 22 μm peaks. These differences in t_{dep} decrease as the scale increases.

The average depletion time of 200 Myr seen across the data is about 5 times smaller than the typical t_{dep} of 1 Gyr in extragalactic studies and larger than the t_{dep} measured for dense clumps. The smaller depletion time for the Galactic Plane than the extragalactic value can be explained by the fact that the 1.1 mm emission used as a gas tracer for this study traces denser gas than the usual gas tracer such as ^{12}CO or ^{13}CO . The 22 μm emission could also be systematically underestimating the SFR across all scales.

We thank Erik Rosolowsky and the rest of the BGPS team for useful discussions and assistance. We thank the referee, Andreas Schruba, for constructive comments that helped improve the paper. This research made use of Montage, funded by the National Aeronautics and Space Administration's Earth Science Technology Office, Computation Technologies Project, under Cooperative Agreement Number NCC5-626 between NASA and the California Institute of Technology. Montage is maintained by the NASA/IPAC Infrared Science Archive. This publication makes use of data products from the Wide-field Infrared Survey Explorer, which is a joint project of the University of California, Los Angeles, and the Jet Propulsion Laboratory/California Institute of Technology, funded by the National Aeronautics and Space Administration. This work was supported by NSF Grant AST-1109116 to the University of Texas at Austin.

REFERENCES

- Aguirre, J. E., Ginsburg, A. G., Dunham, M. K., et al. 2011, *ApJS*, 192, 4
- Anderson, L. D., Bania, T. M., Bialer, D. S., et al. 2014, *ApJS*, 212, 1
- Battersby, C., Bally, J., Ginsburg, A., et al. 2011, *A&A*, 535, A128
- Battersby, C., Bally, J., Jackson, J. M., et al. 2010, *ApJ*, 721, 222
- Battisti, A. J., & Heyer, M. H. 2014, *ApJ*, 780, 173
- Benjamin, R. A., Churchwell, E., Babler, B. L., et al. 2005, *ApJ*, 630, L149
- Bigiel, F., Leroy, A., Walter, F., et al. 2008, *AJ*, 136, 2846
- Blanc, G. A., Heiderman, A., Gebhardt, K., Evans, N. J., II, & Adams, J. 2009, *ApJ*, 704, 842
- Bolatto, A. D., Leroy, A. K., Jameson, K., et al. 2011, *ApJ*, 741, 12
- Calzetti, D., Kennicutt, R. C., Engelbracht, C. W., et al. 2007, *ApJ*, 666, 870
- Calzetti, D., Wu, S.-Y., Hong, S., et al. 2010, *ApJ*, 714, 1256
- Carey, S. J., Noriega-Crespo, A., Mizuno, D. R., et al. 2009, *PASP*, 121, 76
- Churchwell, E., Babler, B. L., Meade, M. R., et al. 2009, *PASP*, 121, 213
- Compiègne, M., Flagey, N., Noriega-Crespo, A., et al. 2010, *ApJ*, 724, L44
- da Silva, R. L., Fumagalli, M., & Krumholz, M. 2012, *ApJ*, 745, 145
- da Silva, R. L., Fumagalli, M., & Krumholz, M. 2014, *MNRAS*, submitted
- Dame, T. M., Hartmann, D., & Thaddeus, P. 2001, *ApJ*, 547, 792
- Draine, B. T., Dale, D. A., Bendo, G., et al. 2007, *ApJ*, 663, 866
- Dunham, M. K., Rosolowsky, E., Evans, N. J., II, Cyganowski, C., & Urquhart, J. S. 2011, *ApJ*, 741, 110
- Dunham, M. K., Rosolowsky, E., Evans, N. J., II, et al. 2010, *ApJ*, 717, 1157
- Ellsworth-Bowers, T. P., Glenn, J., Rosolowsky, E., et al. 2013, *ApJ*, 770, 39
- Ellsworth-Bowers et al. 2014, *ApJ*, submitted
- Evans, N. J., II, Heiderman, A., & Vutisalchavakul, N. 2014, *ApJ*, 782, 114
- Fumagalli, M., da Silva, R. L., & Krumholz, M. R. 2011, *ApJ*, 741, L26
- Gao, Y., & Solomon, P. M. 2004, *ApJ*, 606, 271
- Gao, Y., & Solomon, P. M. 2004, *ApJS*, 152, 63
- Ginsburg, A., Glenn, J., Rosolowsky, E., et al. 2013, *ApJS*, 208, 14
- Heiderman, A., Evans, N. J., II, Allen, L. E., Huard, T., & Heyer, M. 2010, *ApJ*, 723, 1019
- Hildebrand, R. H. 1983, *QJRAS*, 24, 267
- Jackson, J. M., Rathborne, J. M., Shah, R. Y., et al. 2006, *ApJS*, 163, 145
- Jacob, J. C., Katz, D. S., Berriman, G. B., et al. 2010, arXiv:1005.4454
- Jarrett, T. H., Cohen, M., Masci, F., et al. 2011, *ApJ*, 735, 112
- Kennicutt, R. C., & Evans, N. J. 2012, *ARA&A*, 50, 531
- Kennicutt, R. C., Jr. 1998, *ARA&A*, 36, 189
- Kennicutt, R. C., Jr., Calzetti, D., Walter, F., et al. 2007, *ApJ*, 671, 333
- Kruijssen, J. M. D., & Longmore, S. N. 2014, *MNRAS*, 439, 3239
- Lada, C. J., Lombardi, M., & Alves, J. F. 2010, *ApJ*, 724, 687
- Lada, C. J., Lombardi, M., Roman-Zuniga, C., Forbrich, J., & Alves, J. F. 2013, *ApJ*, 778, 133
- Leroy, A., Bolatto, A., Stanimirovic, S., et al. 2007, *ApJ*, 658, 1027
- Leroy, A. K., Walter, F., Sandstrom, K., et al. 2013, *AJ*, 146, 19
- Liu, G., Koda, J., Calzetti, D., Fukuhara, M., & Momose, R. 2011, *ApJ*, 735, 63
- Low, F. J., Young, E., Beintema, D. A., et al. 1984, *ApJ*, 278, L19
- Markwardt, C. B. 2009, *Astronomical Data Analysis Software and Systems XVIII*, 411, 251
- Miville-Deschênes, M.-A., Lagache, G., Boulanger, F., & Puget, J.-L. 2007, *A&A*, 469, 595
- Murray, N. 2011, *ApJ*, 729, 133
- Onodera, S., Kuno, N., Tosaki, T., et al. 2010, *ApJ*, 722, L127
- Ossenkopf, V., & Henning, T. 1994, *A&A*, 291, 943

- Planck Collaboration, Ade, P. A. R., Aghanim, N., et al. 2011, *A&A*, 536, A19
- Rosolowsky, E., Dunham, M. K., Ginsburg, A., et al. 2010, *ApJS*, 188, 123
- Schlingman, W. M., Shirley, Y. L., Schenk, D. E., et al. 2011, *ApJS*, 195, 14
- Schmidt, M. 1959, *ApJ*, 129, 243
- Schruba, A., Leroy, A. K., Walter, F., et al. 2011, *AJ*, 142, 37
- Schruba, A., Leroy, A. K., Walter, F., Sandstrom, K., & Rosolowsky, E. 2010, *ApJ*, 722, 1699
- Shirley, Y. L., Ellsworth-Bowers, T. P., Svoboda, B., et al. 2013, *ApJS*, 209, 2
- Verley, S., Corbelli, E., Giovanardi, C., & Hunt, L. K. 2010, *A&A*, 510, A64
- Vutisalchavakul, N., & Evans, N. J., II 2013, *ApJ*, 765, 129
- Wolynetz, M. S. 1979, *Journal of the Royal Statistical Society. Series C*, 28, 185
- Wong, T., & Blitz, L. 2002, *ApJ*, 569, 157
- Wright, E. L., Eisenhardt, P. R. M., Mainzer, A. K., et al. 2010, *AJ*, 140, 1868
- Wu, J., Evans, N. J., II, Gao, Y., et al. 2005, *ApJ*, 635, L173
- Wu, J., Evans, N. J., II, Shirley, Y. L., & Knez, C. 2010, *ApJS*, 188, 313

TABLE 1
THE DEPLETION TIME AND THE SCATTER IN THE DEPLETION TIME AT EACH RESOLUTION FOR PIXEL-BY-PIXEL ANALYSIS

Resolution(')	$\langle \log t_{\text{dep}} \rangle$			$\sigma(\log t_{\text{dep}})$			$f(\text{limit})$
	fit	limit	EM	fit	limit	EM	
1	8.49	8.30	8.07	0.60	1.00	1.84	0.52
3	8.30	8.30	8.30	0.56	0.75	1.06	0.35
5	8.30	8.33	8.36	0.50	0.60	0.73	0.22
8	8.33	8.34	8.36	0.43	0.48	0.53	0.11
10	8.34	8.34	8.34	0.41	0.41	0.42	0.05
15	8.34	8.34	8.34	0.34	0.31	0.31	< 0.01
20	8.37	8.37	8.34	0.28	0.28	0.28	< 0.01

The average ($\log(t_{\text{dep}})$) and the scatter of the $\log(t_{\text{dep}})$ distribution by three different methods. The *fit* method estimates ($\log(t_{\text{dep}})$) by fitting a log-normal distribution to all data points with positive flux to get the mean and the standard deviation. The *limit* method uses upper limit in Σ_{H_2} and Σ_{SFR} in calculating the median of $\log(t_{\text{dep}})$ and the standard deviation. The *EM* method uses the expectation-maximization algorithm (Wolynetz 1979) to estimate the mean and the standard deviation of censored normal distribution of $\log(t_{\text{dep}})$. The last column, $f(\text{limit})$ gives the fraction of the data points with an upper limit on either Σ_{H_2} or Σ_{SFR} .

TABLE 2
PARAMETERS FOR THE SOURCE BASED ANALYSIS

Resolution	1.1 mm					
	ρ	$\rho(\text{rank})$	robust(n, a)	LS(n, a)	$\log(t_{\text{dep}})$	$\sigma(\log(t_{\text{dep}}))$
10'	0.66	0.63	0.97, -2.4	0.65, -2.1	8.43	0.34
15'	0.65	0.62	0.91, -2.2	0.59, -1.9	8.34	0.32
20'	0.76	0.79	0.84, -2.1	0.63, -1.9	8.32	0.24
Resolution	22 μm					
	ρ	$\rho(\text{rank})$	robust(n, a)	LS(n, a)	$\log(t_{\text{dep}})$	$\sigma(\log(t_{\text{dep}}))$
10'	0.70	0.66	0.94, -2.3	0.66, -2.0	8.37	0.34
15'	0.67	0.64	1.0, -2.5	0.71, -2.1	8.41	0.31
20'	0.84	0.83	1.0, -2.5	0.87, -2.3	8.45	0.21
Resolution	Bolocat					
	ρ	$\rho(\text{rank})$	robust(n, a)	LS(n, a)	$\log(t_{\text{dep}})$	$\sigma(\log(t_{\text{dep}}))$
33''	0.50	0.40	0.84, -2.68 ^a		9.20 ^b	0.59 ^b

Note: (a) linear fit to the data using MPFITEXY (Marhwadt, 2009).

(b) Values correspond to mean and standard deviation of $\log(t_{\text{dep}})$ from the expectation-maximization (EM) method.

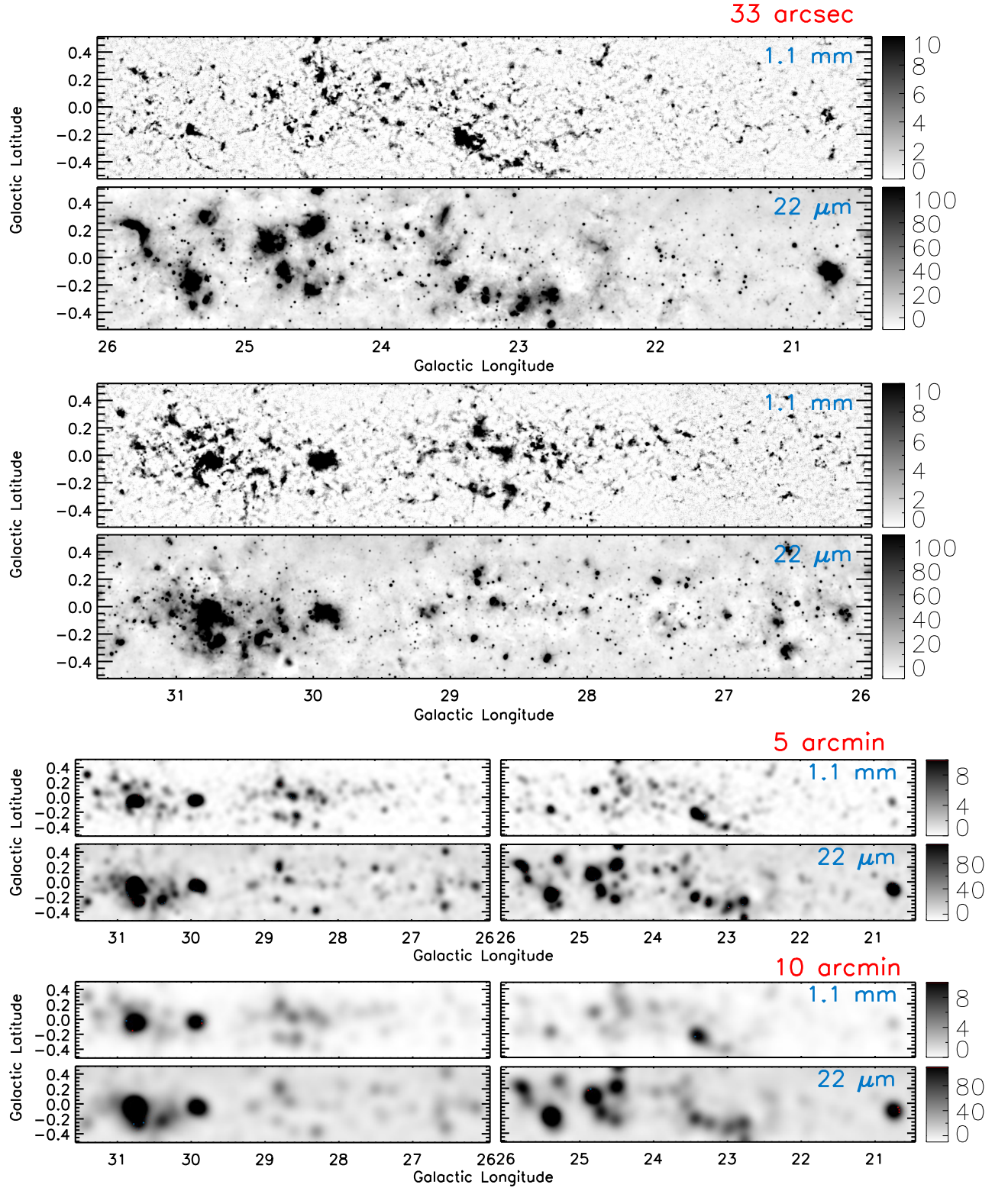


FIG. 1.— BGPS 1.1 mm and WISE 22 μm images for the entire region at three different resolutions of 33'' (top 4 panels), 5' (middle 4 panels), and 10' (bottom 4 panels).

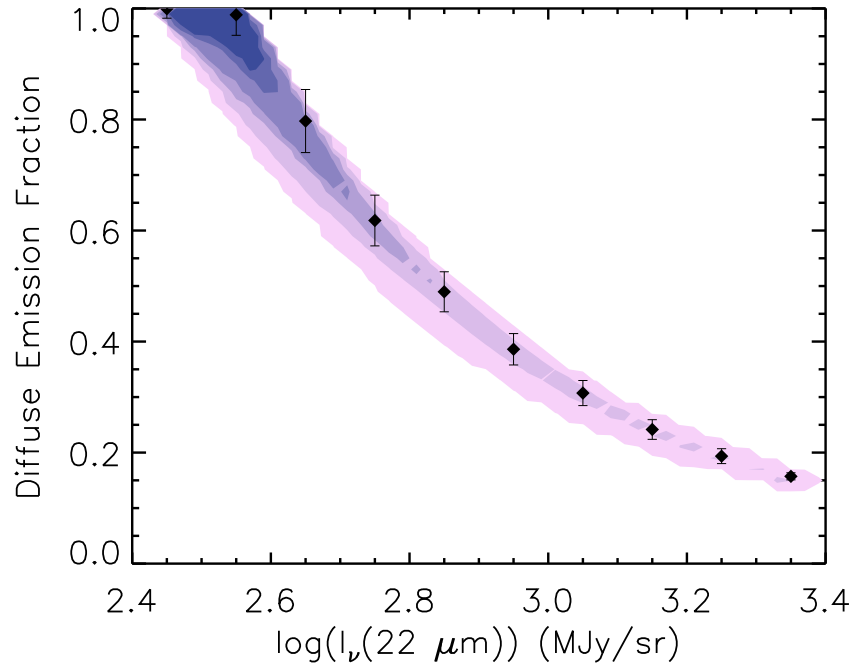


FIG. 2.— The fraction of the diffuse (cirrus) emission in WISE 22 μm image shows a large contribution from the diffuse emission to the total flux at low surface brightness regions. Each data point and the error bar represent a median and a standard deviation of the diffuse emission over total emission inside a bin of $\log(I_\nu(22 \mu\text{m}))$ with a bin size of 0.1. The color contours represent pixel number density contours.

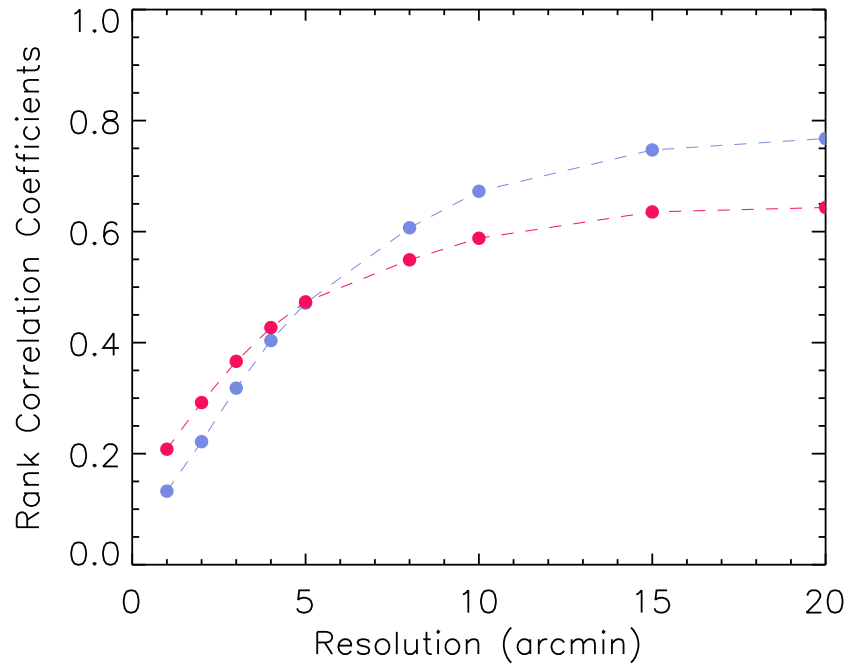


FIG. 3.— The pixel-by-pixel rank correlation coefficients between 1.1 mm images and 22 μm images increase steeply at small scales and asymptote around 5-8' for both regions. The blue data points represent the correlation coefficients from region 1, and the red data points represent region 2.

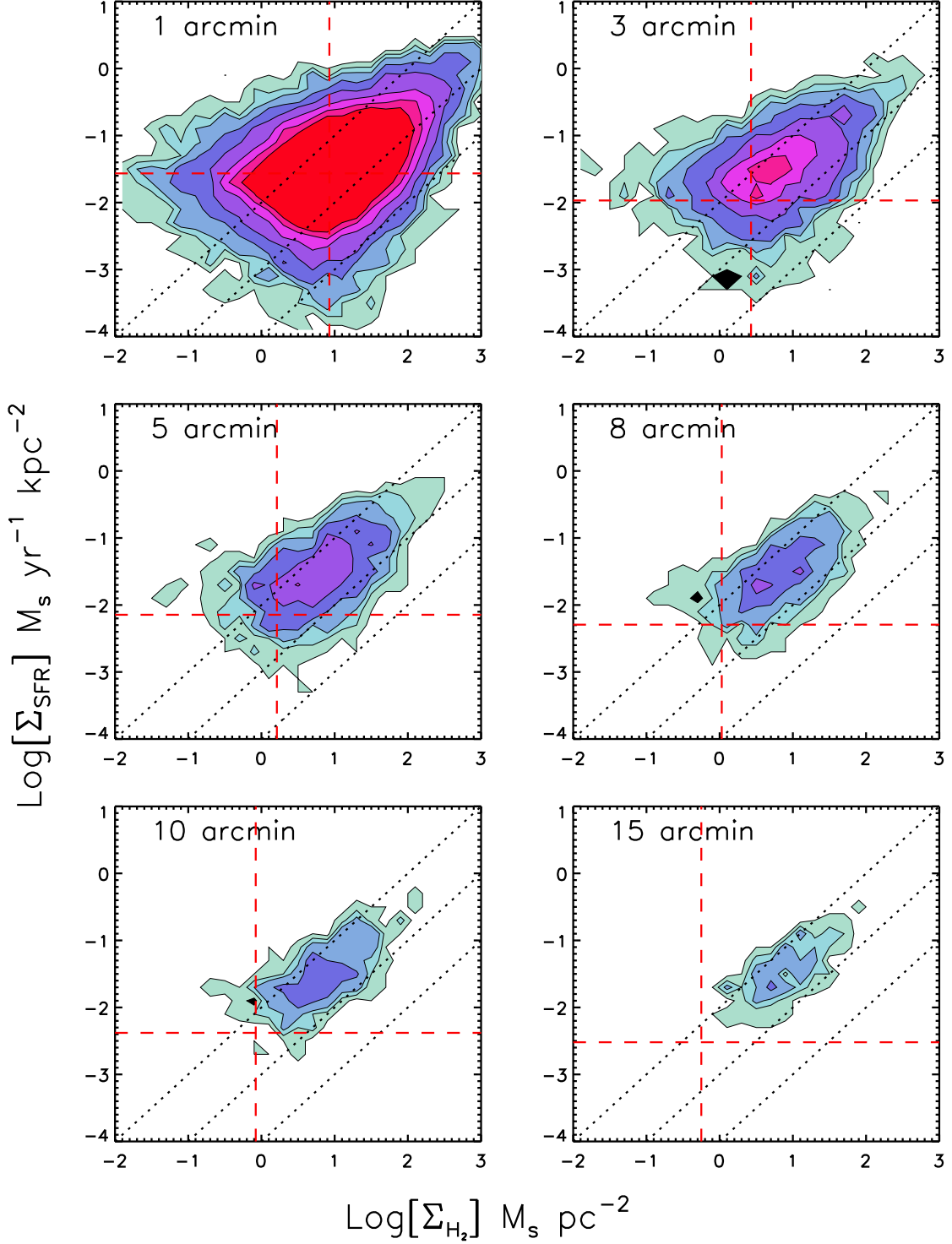


FIG. 4.— The pixel-by-pixel star formation relations of Σ_{H_2} and Σ_{SFR} at different resolutions show large scatters at small scales and tighter relations at larger scales. The contours represent source number densities of 1, 3, 5, 10, 20, 40, 60, and 80 data points at the binning of 0.2 in Σ_{H_2} and Σ_{SFR} . The same color represents the same number density in all the plots. The three dotted lines show lines of constant depletion time with $t_{\text{dep}} = 10^8, 10^9, 10^{10}$ yr from top to bottom. The horizontal and vertical dashed lines show the 3-sigma detection limit for Σ_{SFR} and Σ_{H_2} respectively.

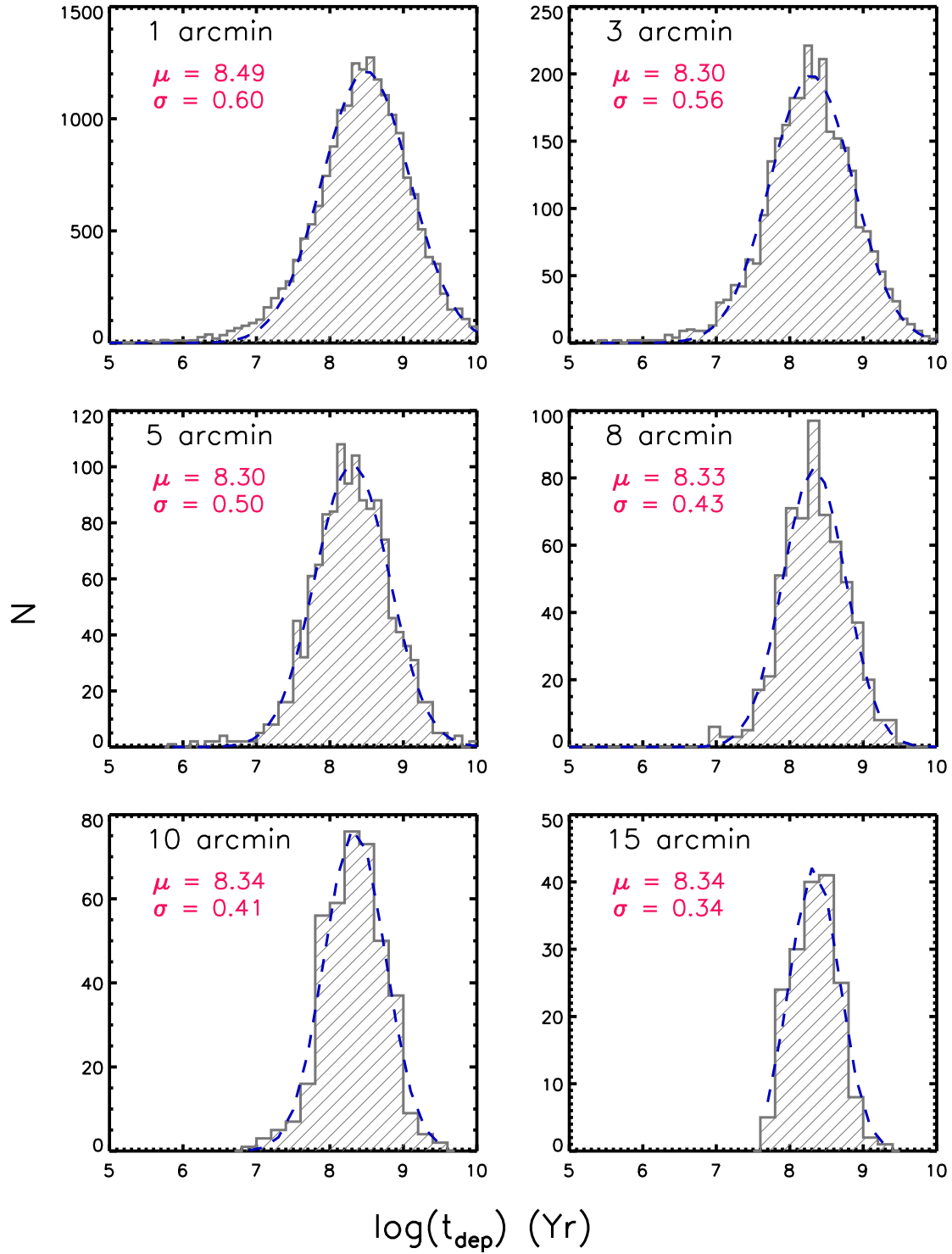


FIG. 5.— The distributions of $\log(t_{\text{dep}})$ for all the regions with positive 1.1 mm and 22 μm flux at the scales of 1', 3', 5', 8', 10', and 15' are shown in grey. The dashed, blue line in each plot represents a Gaussian fit to the distribution. The mean (μ) and the standard deviation (σ) from the Gaussian fit are shown in red for each plot. The mean t_{dep} from the fit does not change much at different scales, while the standard deviation decreases as the scale increases.

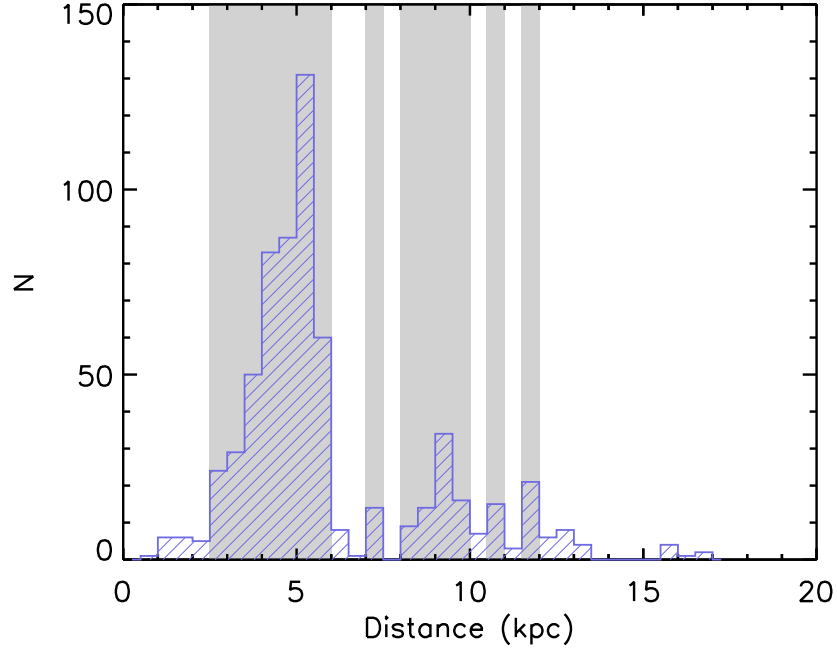


FIG. 6.— The distribution of the distances to a subset of the Bolocat sources inside our target regions from Ellsworth-Bowers et al. (2014) shows a large fraction of the sources locate around 5 kpc, and a smaller fraction of the sources locate around 10-12 kpc. The mean of the distances is 5.9 kpc, and the median is 5.1 kpc. The shaded grey area represents the area inside which the number of sources accounts for 90% of the total sources.

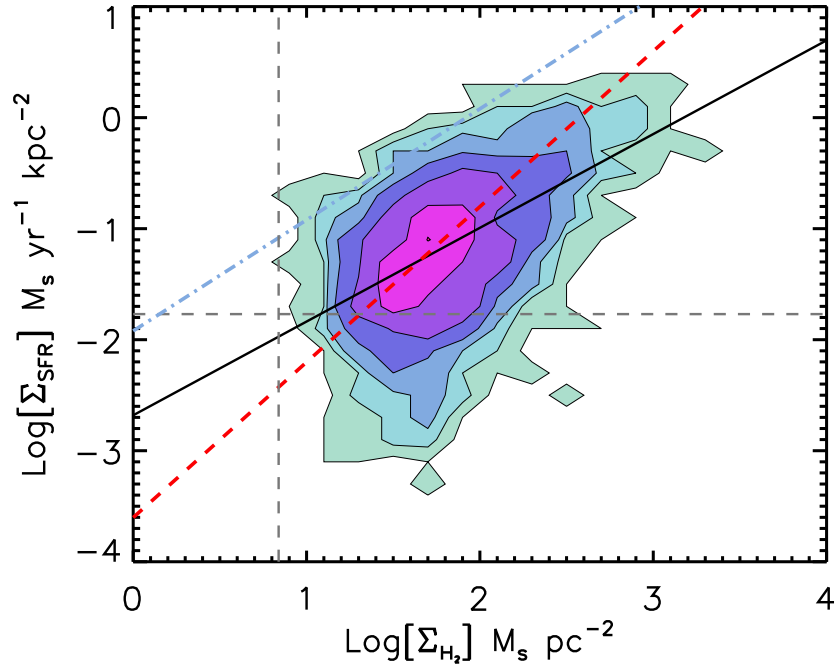


FIG. 7.— The star formation relation for Bolocat sources with a photometry aperture radius of $40''$ shows a weak relation with a large scatter. The contours represent the same source number densities as in Figure 4. The solid black line represents the best linear fit to the log of the data while the dashed, red line represents the extragalactic star formation relation (Equation 6), and the dot-dashed blue line represents the Galactic relation for dense gas from Wu et al. (2005). The vertical and the horizontal grey, dashed lines show the 3-sigma detection limit in Σ_{H_2} and Σ_{SFR} respectively.

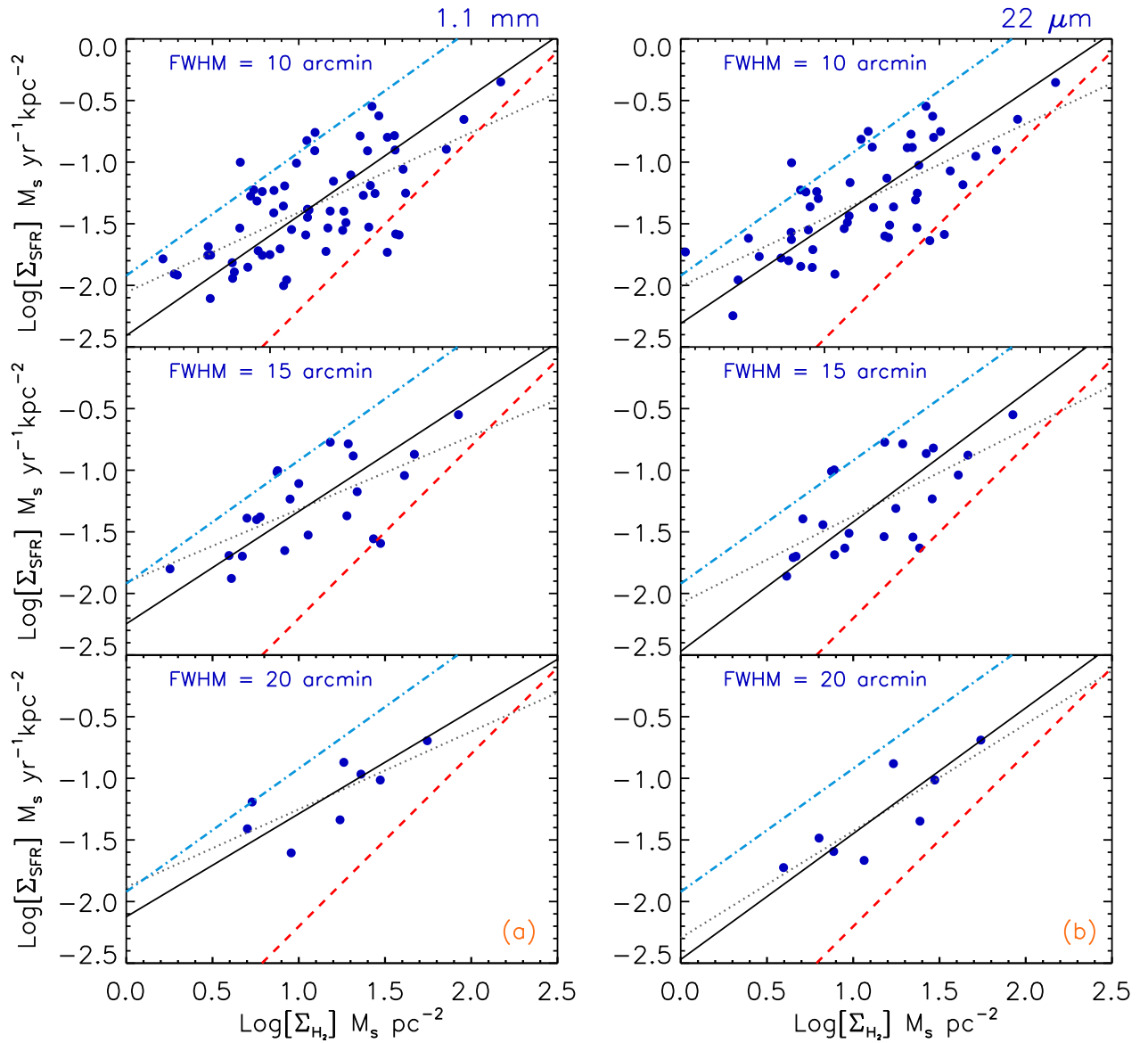


FIG. 8.— Σ_{SFR} versus Σ_{H_2} from aperture photometry centered at 1.1 mm peaks (a) and 22 μm peaks (b) for image resolutions of 10', 15', and 20'. The solid black line in each plot represents a robust linear fit to the data while the dotted grey line represents a least-square fit. The dashed red line represents the extragalactic relation from Kennicutt et al. (1998) and the dot-dashed blue line is the dense gas relation from Wu et al. (2005).

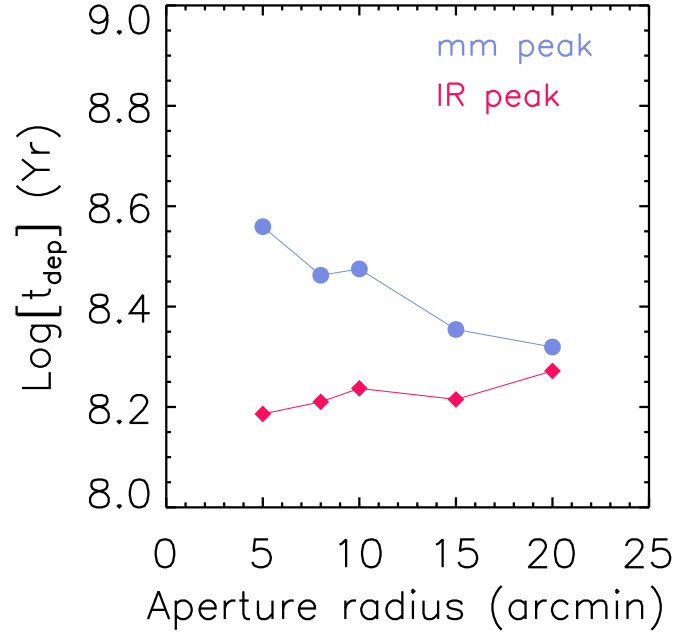


FIG. 9.— Comparing the average depletion time between two methods of selecting regions show that the average t_{dep} is larger for regions centered at 1.1 mm peaks than for regions centered at $22 \mu\text{m}$ peaks when cuts of 100 signal-to-noise ratio were applied to Σ_{H_2} and Σ_{SFR} .

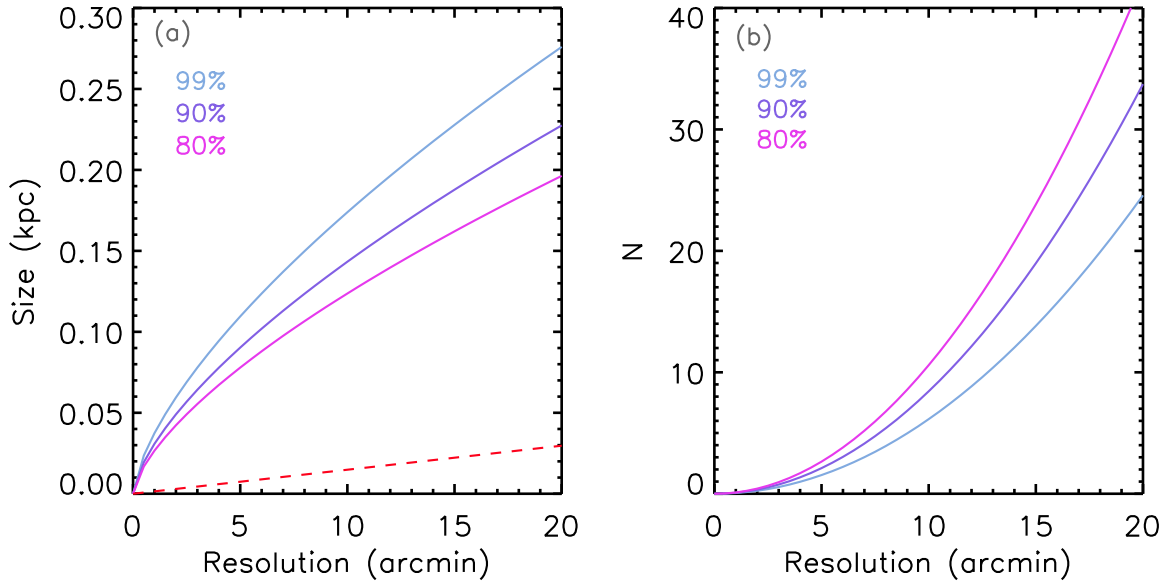


FIG. 10.— (a) Effective averaging scales as a function of angular resolution estimated by using a median distance of 5.1 kpc and distance ranges corresponding to source percentage of 80%, 90%, and 99% of total sources. The dashed red line shows the transverse physical sizes at a distance of 5.1 kpc. (b) Estimated number of 1.1 mm sources inside one resolution element for areas covering source percentage of 80%, 90%, and 99% of total sources.

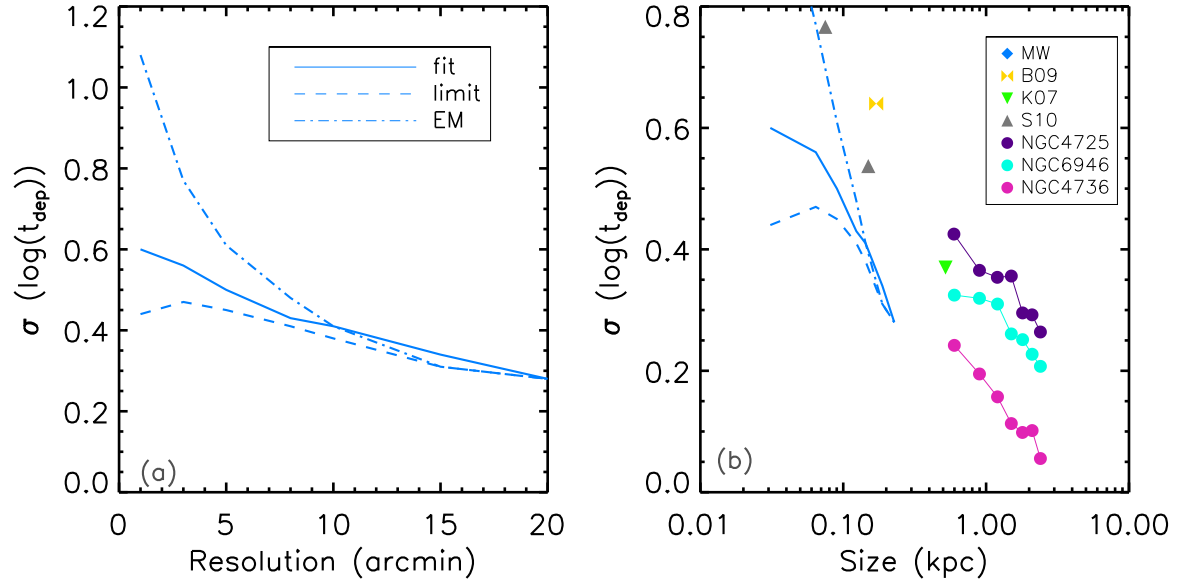


FIG. 11.— (a) The standard deviation of the $\log(t_{\text{dep}})$ at different scales, calculated by three different methods for the pixel-by-pixel analysis. *fit* shows the result from a Gaussian fit to the distribution of $\log(t_{\text{dep}})$ for all data points with positive flux. *limit* refers to the standard deviation of the $\log(t_{\text{dep}})$ after upper limits were assigned to Σ_{H_2} and Σ_{SFR} . *EM* refers to the standard deviation from the expectation-maximization method, which estimated the censored data assuming a normal distribution of $\log(t_{\text{dep}})$. (b) Comparisons of the standard deviation of the $\log(t_{\text{dep}})$ between the Galactic Plane from this study and the extragalactic studies of M51(a) by Blanc et al. 2009 (B09), NGC5194 by Kennicutt et al. 2007 (K07), M33 by Schruba et al. 2010 (S10), and Leroy et al. 2013 (NGC4725, NGC6946, NGC4736). All the data for extragalactic studies were taken from Leroy et al. (2013)

APPENDIX

A. SATURATION

WISE 22 μm images contain some saturated regions with a large number of saturated pixels near peaks of bright, extended emission. The saturated areas are small compared to the total area, but saturation will affect larger portions of the image once we convolve to larger beam sizes. For further analysis, we replaced the saturated pixels with estimated values. Over an extended saturated region, the estimation was done by calculating average values of the surrounding regions and performing a thin plate spline interpolation. Consequently, the values of the flux over saturated regions have large uncertainties. However, the saturated area only covers less than 0.01 percent of the entire image. The uncertainties in the estimations should have minimal effect on the flux calculations.

B. PHOTOMETRIC UNCERTAINTY

The uncertainties in the Σ_{SFR} for the Bolocat sources (§5.2) came from the estimated uncertainties in the photometry performed on WISE 22 μm images. Since the photometry was performed directly from the WISE all-sky release images, the uncertainties were estimated following the Explanatory Supplement to the WISE All-Sky Data Release Products. The uncertainty of the source flux (σ_{src}) was contributed by instrumental and calibrational uncertainties, Poisson noise, and uncertainties from background estimations. The σ_{src} was estimated by:

$$\sigma_{\text{src}}^2 = F_{\text{corr}} \left(\sum \sigma_{iA}^2 + \frac{N_A^2}{N_B} \sigma_{\text{B/pix}}^2 \right),$$

where

- F_{corr} = pixel to pixel correlated noise correction factor
- σ_{iA} = flux uncertainty for each pixel inside the aperture
- $\sigma_{\text{B/pix}}$ = uncertainty in the background per pixel
- N_A = number of pixels inside the aperture
- N_B = number of pixels used to estimate the background flux.

After obtaining the 22 μm mosaics for the two regions, the images were convolved to a resolution of $33''$ to match the resolution of the 1.1 mm images from BGPS. σ_{iA} were obtained from the original uncertainty maps from the WISE all-sky release. The correction for correlated noise, F_{corr} , was obtained from the WISE Explanatory Supplement, for which it has been estimated for certain aperture sizes. The background flux was estimated by the method described in §3.1. In creating the background images, several parameters were chosen to give a result that was representative of the diffuse emission.

(i) A subgrid size was chosen over which one local background level was estimated. The chosen value was 200 pixels, and comparison values are 100, 150, 250, and 300 pixels. (ii) A clipping factor was chosen so that grids with source area larger than the clipping factor were omitted. The chosen value was 0.3, and comparison values are 0.1, 0.2, 0.4, and 0.5. (iii) The threshold value for the source flux was chosen. All pixels with flux value above the threshold were considered source regions. The chosen value was 1.0, and comparison values are 0.5 and 1.5.

How the changes in these parameters affect the resulting background estimations was considered in the estimations of $\sigma_{\text{B/pix}}$. We calculated $\sigma_{\text{B/pix}}$ by changing the three parameters around the chosen values and created the background images. We then compared the resulting images to the chosen background images. The differences between two background images were quantified by

$$\sigma_{\text{diff}}^2 = \frac{1}{N} \sum_{i=1}^N (f_i - f'_i)^2,$$

where N is the number of pixels in the image, f_i is the pixel flux of the chosen image, and f'_i is the pixel flux for the comparison image. σ_{diff}^2 were calculated for all the comparing background images and the average of the results was adopted as the value for $\sigma_{\text{B/pix}}^2$. To see how our estimation of $\sigma_{\text{B/pix}}$ compared to the spatial variations of the flux, we looked at the pixel flux distribution of the background subtracted 22 μm image of region 1. Figure 12 shows the pixel flux distribution of region 1. To fit the pixel noise variations, we reflected the negative flux distribution about zero and fitted a Gaussian distribution. The resulting fit is shown as the orange dashed line in the figure. The fitting gave a Gaussian distribution parameters of $\sigma = 0.001$ Jy/pixel. At the aperture size of $80''$, the noise corresponds to $\sigma \approx 0.02$ Jy/source. Our estimation of $\sigma_{\text{B/pix}}$ for region 1 gave $\sigma \approx 0.11$ Jy/source.

C. COMPARING METHODS OF DIFFUSE IR BACKGROUND ESTIMATIONS

Our method of estimating diffuse 22 μm emission is described in §3.1. Figure 13 shows the WISE 22 μm images for region 1 before and after diffuse background subtraction. We compared our method to the cirrus removal method from Battersby et al. (2011, hereafter B11). B11 estimated diffuse emission for the Herschel 500 μm emission. The

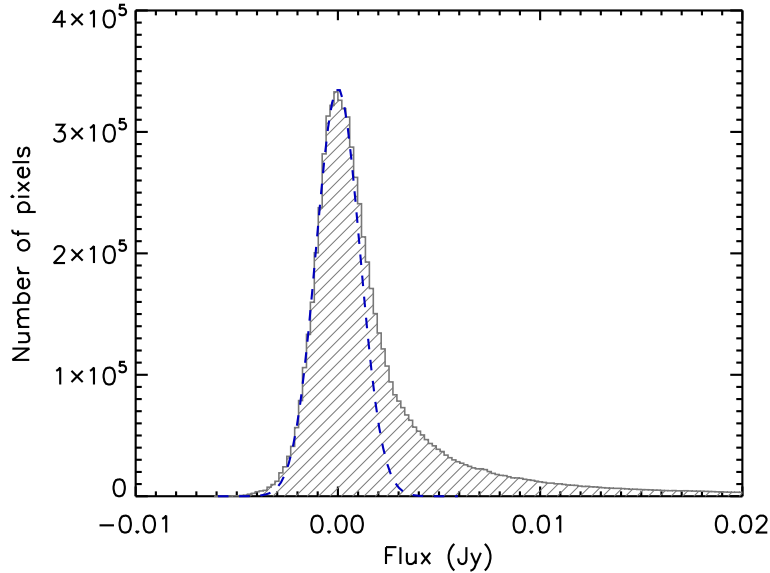


FIG. 12.— Pixel flux distribution for $22 \mu\text{m}$ image of region 1. The blue dashed line shows the Gaussian fit to the flux distribution of flux < 0 and a reflected image of the negative flux for flux > 0 .

brief summary of the method is as follow. The original image was convolved with a Gaussian beam; then a Gaussian fit was performed in the Galactic latitude at each of the Galactic longitude. The fitted image was subtracted from the original image. The subtracted image was used for estimating a cutoff (4.25σ) of source flux so that everything above the cutoff was considered as sources. Area above the cutoff was masked out in the original image. The process was then iterated until the source mask cutoff converges. The original image was masked out with the final cutoff value and convolved with a Gaussian kernel to create a background subtracted image.

We compared the background images of region 1 from our method with the method of B11 performed on the same region of the WISE $22 \mu\text{m}$ image using a Gaussian kernel $\text{FWHM} = 12'$. The result shows that the background image from B11 method gave a comparable background to our method with slightly stronger background in bright source area. Figure 14 shows a histogram of $(\text{our background image} - \text{B11 background image}) / (\text{original } 22 \mu\text{m image})$. The fractional differences are small with the highest absolute value of 0.04. This result indicates that the choice of a method of background subtraction does not significantly affect the photometric flux.

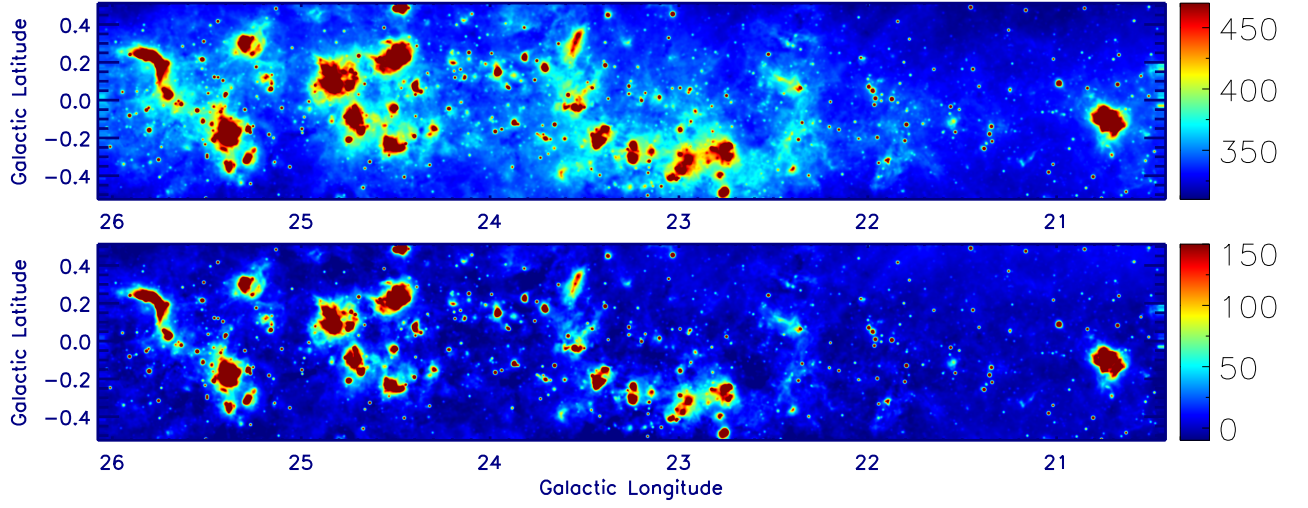


FIG. 13.— WISE $22\ \mu\text{m}$ image of region 1. The top image shows the original mosaic, and the bottom image shows the background-subtracted mosaic. The color bar is in the unit of MJy/sr.

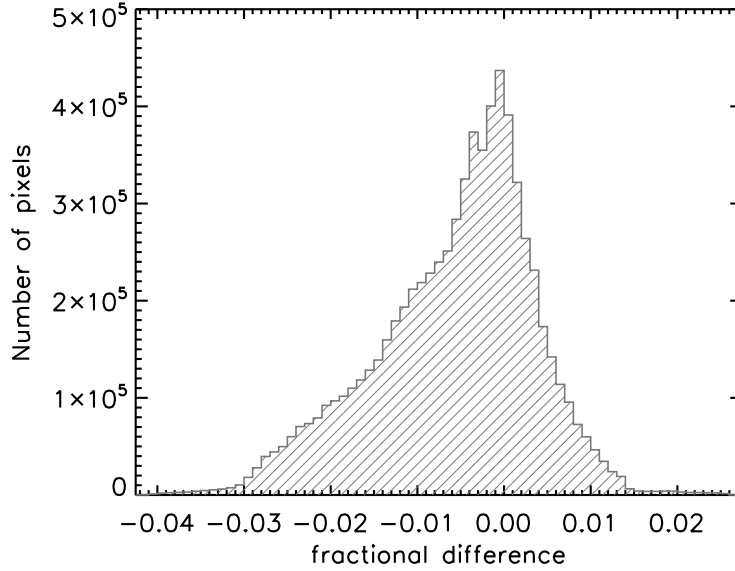


FIG. 14.— A comparison between two methods of background estimations for the $22\ \mu\text{m}$ image of region 1. The fractional difference is the ratio of the difference between our background image and B11 background image over the original $22\ \mu\text{m}$ image.